



DEGREE PROJECT IN ENGINEERING PHYSICS,
SECOND CYCLE, 30 CREDITS
STOCKHOLM, SWEDEN 2020

Polarization stabilization for quantum key distribution in deployed fibre

LISELOTT EKEMAR

KTH ROYAL INSTITUTE OF TECHNOLOGY
SCHOOL OF ENGINEERING SCIENCES

Polarization stabilization for quantum key distribution in deployed fibre

Liselott Ekemar

Master in Engineering Physics

Date: 15 August 2020

Supervisor: Katharina Zeuner and Samuel Gyger (KTH), Dr. Gemma
Vall-llosera (Ericsson)

Examiner: Prof. Val Zwiller

School of Engineering Sciences

Host company: Ericsson AB

Swedish title: Polarisationsstabilisering för kvantnyckeldistribution i dragen
fiber

Abstract

Quantum key distribution is a method for transmitting a cryptographically encrypted key with unbreakable security based on the laws of quantum mechanics. Using quantum key distribution would revolutionise it-security, and prepare the technology for a future with quantum computers. A distribution channel for quantum key distribution, a quantum network is necessary for entering the quantum era. In this network the carrier of quantum properties will be distributed, the favourite medium as information carrier being photons, with the information encoded in the polarization. However, the polarization is exposed to disruptions due to birefringence in optical fibres, causing polarization rotation.

In this thesis we have characterised the polarization drift in 8 km of deployed standard single mode (SSMF28) optical fibre between the Quantum Nano Photonics lab at Albanova university center and Ericsson lab in Kista. The polarization drift was slow with an average change of $0.759\% \pm 0.409\%$ per hour. Further, three waveplates (two quarter waveplates and one half waveplate) that will be used in the proposed polarization stabilisation setup have been characterised with a local laser. This showed that the characterised waveplates are not perfect and their induced polarization deviation of $28.889\% \pm 0.519\%$ from the theoretical value was observed. A polarization controlling algorithm was implemented. However, based on the discrepancy between ideal and real waveplates, the output from the polarization controlling algorithm produced a polarization deviation of $78.087\% \pm 0.222\%$. Future improvements to enable QKD applications will be discussed

Sammanfattning

Kvantnyckeldistribution är en överföringsmetod av nycklar med obrytbar kryptering baserad på kvantmekaniskens lagar. Användandet av kvantnyckeldistribution skulle revolutionera it-säkerheten och förbereda teknologin för en framtid med kvantdatorer. Kvantnyckeldistribution kräver en distributionskanal, ett kvantnätverk, vilke är en nödvändighet för kvanttidsåldern. I detta nätverk kommer bärare av kvantegenskaper att bli distribuerad. Favoritbäraren av dessa kvantegenskaper är fotoner, med informationen inkodad i polarisatinen. Men polarisation är utsatt för störningar inducerade av reflektionen i de optiska fibrerna, vilket orsakar rotering av polarisationen. I detta arbete presenterar vi karakteriseringen av polarisationsdriften inducerad av en 8 km lång standard singelmode fiber (SSMF28) mellan kvant- och nanofotoniks labbet i Alba Nova universitetscentrum och Ericsson lab i Kista. Den uppmätta polarisationsdriften var långsam med en genomsnittlig förändring av $0.759\% \pm 0.409\%$ per timme. Vidare var tre vågplattor (två kvartsvågsplattor och en halvvågsplatta) karaktäriserad med hjälp av en lokal laser. Dessa mätningar visade att den inducerade polarisationen skiljde sig $28.889\% \pm 0.519\%$ från de teoretiska värdena. Dessa vågplattor användes sedan i en förslagen setup för polarisations stabilisering. För att kontrollera denna setup var en polarisationskontrollerande algorim implemented. På grund av skillnaden mellan ideala vågplattor och de använda vågplattorna så skiljde sig polarisationen upp till $78.08\% \pm 0.222\%$ från den teoretiska polarisationen. Framtida förbättringar för att öka möjligheterna till tillämpningar av kvantnyckeldistribution kommer att diskuteras.

Acknowledgements

I want to thank my supervisors Katharina Zeunert and Samuel Gyger for providing the background, support and advice. Katharina for your help with the physical setup and your reading and commenting on everything I have been writing, whatever it made it to this thesis or not. Samuel for your software development support and your thoughts about how to move on to the next step of the project when things have not worked out as planned. I would also like to thank my supervisor Dr. Gemma Val-llosera This project would not have been possible without you. Your enthusiasm for the subject and the support relating to practical issues has been invaluable. I would also want to extend my thanks to the Innovation and Incubation team for the warm welcome to the organisation.

I also would like to thank Patrick Usher for providing a network for the lab computer and enabling remote control via the network. And in addition, for the help with practical issues during my work with the setup. Thanks also to Robert Gouffrich for enabling access to Ericsson lab and giving us a suitable place for the lab setup.

A special thanks also to Dr. Lucas Schweickert for your patient supervising of me in an optics lab before my thesis project started. Working alone with the optics setup at Ericsson would have been a much more fearful experience without the time under your supervision. I would also like to thank Dr. Klaus Jöns for the help of sorting out an error message from the PI-stages. Thanks to Prof Val Zwiller for organizing this project together with Gemma, as well as your interest in every step of this project and formulating the long term goal of the project this thesis is a part of.

I would finally want to thank Rasmus for all you love and support during this strange spring and summer, but also through the time at KTH. I would also like to extend this thank to my family and friends for bringing perspective into my studies and sometimes managing to make me take a break.

Contents

1	Introduction	5
2	Background	7
2.1	Polarization stabilisation	7
2.1.1	Polarization	7
2.1.2	Polarization rotation	10
2.1.3	Polarization transform to an arbitrary state of Polarization	13
2.1.4	Polarization control	14
3	Method	15
3.1	The fibre link	15
3.2	Setup components	15
3.2.1	Polarimeter	15
3.2.2	Polarization controller	17
3.2.3	Light filtering	17
3.3	Setups	17
3.3.1	Polarization drift measurement	17
3.3.2	Waveplate characterisation	18
3.3.3	Initial setup for polarization control	19
3.3.4	Final setup for polarization control in Ericsson lab	20
3.4	polarization controlling algorithm	20
3.5	Error calculations	21
4	Results and discussion	22
4.0.1	Polarization drift measurements	22
4.1	Waveplate characterisation	25
4.1.1	Characterisation of HWP	26
4.1.2	Characterisation of quarter waveplate 1	30
4.1.3	Characterisation of quarter waveplate 2	33
4.2	Waveplate characterisation using the final setup	37
4.3	Polarization control	39
5	Conclusion and outlook	49

List of Figures

2.1	polarization ellipse with the parameters describing the ellipse. χ is measured as the angle between the slow axis and the polarization vector, θ is the angle between the horizontal axis and the polarization vector.	8
2.2	The Poincaré sphere with the Stokes parameters visualised along the corresponding axis.	10
2.3	Horizontally polarised light propagates through a HWP with the fast axis aligned with the V-axis.	11
2.4	Horizontal polarised light propagates through a QWP with the fast axis aligned with the V-axis.	12
2.5	Schematic diagram of the polarization transforming system.	13
3.1	The polarimeters used for polarization measurements.	16
3.2	The setup used for measurement of the uncontrolled polarization drift. The laser in QNP lab launches a light beam into a fibre, this light beam is then splitted by a beamsplitter. The weak arm of the splitted light beam ins leads to the PAX5710 Polarimeter at the QNP lab. The strong arm is lead though the fibre link to Ericsson lab. The light beams SOP is measured with the PAX1000 polarimeter in the Ericsson lab. Image source [1]	18
3.3	Setup used for characterisation of the waveplates. Blue link indicates a fibre link, red links indicate FSO (free space optical) link. After collimating the laser light, the beam propagates through a polariser, one QWP and one HWP. Thereafter propagates the light beam through the WP of interest for characterisation before the polarization is measured by the polarimeter.	18
3.4	Initial setup used for polarization control. Grey links identify fibre based connections and red links are used for FSO. A laser in the QNP lab launches the lightbeam into the optical fibre. The light beam propagates through the fibre link to the Ericsson lab. There the collimator will launch the light into the FSO link. Thereafter, the light beam propagates through the polarization controller, which can change the SOP. Finally, the SOP is measured by the polarimeter. Image source [1]	19
3.5	The final setup, which allows the polarization control to be combined with single photon counting technology. Here paired with a local laser.	20
4.1	The polarization drift at QNP lab and Ericsson labs, measured during 15-19 May 2020. The stoke vectors are normalised for visualisation of the polarization on the Poincaré sphere.	22

4.2	polarization drift, measured 15-19 May 2020. the polarization at QNP in (a) and the drift of the polarization after travelling through the fibre link in (b). The normalised Stokes parameters are individually plotted against the time at the x-axis. This enables easy visualisation of the chronology of the polarization drift induced by environmental variations which impact the fibre link.	24
4.3	The power drift at QNP lab and Ericsson lab during the polarization drift measurement 15-19 May 2020, normalised with the min-max feature scaling. The y-axis shows the normalised power, and the x-axis the time.	25
4.4	Characterisation of the HWP, where the input SOP has the V-state. The measured output SOP is compared with the output SOP produced by an ideal HWP.	26
4.5	Characterisation of the HWP, where the input SOP has the H-state. The measured output SOP is compared with the output SOP produced by an ideal HWP.	27
4.6	Characterisation of the HWP, where the input SOP has the L-state. The measured output SOP is compared with the output SOP produced by an ideal HWP.	28
4.7	Characterisation of the HWP, where the input SOP has the R-state. The measured output SOP is compared with the output SOP produced by an ideal HWP.	29
4.8	Characterisation of the QWP 1, where the input SOP has the V-state. The measured output SOP is compared with the output SOP produced by an ideal QWP.	30
4.9	Characterisation of the QWP 1, where the input SOP has the H-state. The measured output SOP is compared with the output SOP produced by an ideal QWP.	31
4.10	Characterisation of the QWP 1, where the input SOP has the L-state. The measured output SOP is compared with the output SOP produced by an ideal QWP.	32
4.11	Characterisation of the QWP 1, where the input SOP has the R-state. The measured output SOP is compared with the output SOP produced by an ideal QWP.	33
4.12	Characterisation of the QWP 2, where the input SOP has the R-state. The measured output SOP is compared with the output SOP produced by an ideal QWP.	34
4.13	Characterisation of the QWP 2, where the input SOP is L-polarised. The measured output SOP is compared with the output SOP produced by an ideal QWP.	35
4.14	Characterisation of the QWP 2, where the input SOP has the H-state. The measured output SOP is compared with the output SOP produced by an ideal QWP.	36
4.15	Characterisation of the QWP 2, where the input SOP has the V-state. The measured output SOP is compared with the output SOP produced by an ideal QWP.	37
4.16	Characterisation of the HWP and QWP 2 using the final setup in Ericsson lab and a local laser.	38
4.17	The polarization of the input SOP, which is the original SOP. This is the normalised SOP of the lightbeam before it is sent through the fibre link to the Ericsson lab.	39
4.18	The data for the correction of the polarization in a light beam, which has been sent from QNP lab to Ericsson lab, measured at Ericsson lab. The corrected output SOPs goal state is the H-state.	40
4.19	The data for the correction of the polarization in a light beam, which has been sent from QNP lab to Ericsson lab, measured at Ericsson lab. The corrected output SOPs goal state is the R-state.	41
4.20	The data for the correction of the polarization in a light beam, which has been sent from QNP lab to Ericsson lab, measured at Ericsson lab. The corrected output SOPs goal state is the D-state.	42
4.21	The data for the correction of the polarization in a light beam, which has been sent from QNP lab to Ericsson lab, measured at Ericsson lab. The corrected output SOPs goal state is the A-state.	44

4.22 The data for the correction of the polarization in a light beam, which has been sent from QNP lab to Ericsson lab, measured at Ericsson lab, measured at Ericsson lab. The corrected output SOPs goal state is the L-state.	46
4.23 The data for the correction of the polarization in a lightbeam, which have been sent from QNP lab to Ericsson lab, measured at Ericsson lab, measured at Ericsson lab. The corrected output SOPs goal state is the V-state.	47

Chapter 1

Introduction

The demand for sending encrypted information has never been as large as in the contemporary time, but commonly used encryption methods cannot guarantee ultimate security to be broken. During most of history, the need for encryption has been limited to military information, communication within secret services and a few business secrets. But in the current information era has the question of good encryption been a part of the everyday life, for logging on to the bank, updating licenses, sending e-mails with sensitive information and online tax reports. Despite the demand for safe encryption, and the increasing amount of encrypting methods, only one method has proven to be unbreakable. This method requires the use of a one-time pre-shared key, of the same length as the message of interest. This method called one-time pad encryption and was invented by Vernam in 1919 and was shown by Shannon in 1949 to be the only encryption method which is unbreakable [2, 3]. Although this is the only unbreakable encryption method, it is rarely used since it is impractical for longer messages and a new key must be shared for every new message. This sharing of keys must also be done with a safety level making sure the key is not eavesdropped, which means that the key must be physically shared. The one-time pad encryption is therefore not a feasible encryption method in modern IT-security.

The commonly used encryption methods are not unbreakable but constructed under the assumption that their complexity protects the message from eavesdropping, but eavesdropping can not be excluded, therefore would a feasible unbreakable encryption method revolutionise the field of IT-security. This revolution is offered by encryption methods relying on the foundation of quantum mechanics. These encryption protocols rely on the no-cloning theorem, which states that an arbitrary quantum state can not be cloned [4]. The ground for this type of cryptography was laid by the BB84-protocol, invented by Bennet and Brassard in 1984, and the E91-protocol, invented by Ekert in 1991. The BB84-protocol, considers a scenario where Alice sends an encrypted quantum key in one of four possible bases, and Bob measures the quantum key in one of four possible bases. Alice and Bob will then compare their measurements and only keep the bits measured in the same basis. This result is the sifted key, which Alice and Bob openly compare a part of a part of to make sure they are identical. If they are not, they know that an eavesdropper has been present [5]. A similar protocol was invented by Ekert in 1991 when he suggested a protocol using entangled properties created by a source separate from as well Alice and Bob as a potential eavesdropper. Alice and Bob will receive one carrier of the entangled quantum property from each pair, and perform correlation measurements of these. If Alice and Bob are eavesdropped using this protocol, the entanglement measurement will not show quantum mechanical correlation and the eavesdropping will be revealed [6]. These protocols discussed above are the ground for quantum key distribution (QKD), which is

the name for encryption based on quantum informatics [7].

Practical applications of QKD require a network that enables the distribution of quantum states between users [8]. Since a global network of optical fibres already exists for internet provision, photons are a natural choice as information carriers in a quantum network [9]. Photons have multiple quantum properties such as frequency, phase and polarization. Frequency and phase could be preferred carrier since these, unlike polarization, are naturally protected from disruptions induced by birefringence in optical fibre. These disruptions, which causes a polarization rotation is not static, but varies over time. The polarization rotation is therefore rather a polarization drift, induced by environmental factors, such as temperature [10]. Despite the polarization drift, for implementations where multiple users share the same bandwidth, the polarization is superior to other alternatives since encoding in frequency or phase requires interferometers for detection, which increases the complexity of the system [11]. If the environmental factors are kept stable, entanglement between photons can be proved over long distances [12]. However, to be able to perform similar measurements in any deployed fibre, a polarization controlling setup, which compensates for the polarization drift, is required.

Chapter 2

Background

2.1 Polarization stabilisation

2.1.1 Polarization

According to Maxwell equations, the time-independent complex amplitude of light along the z-axis can be described by

$$U(\mathbf{r}) = u(\mathbf{r}) \exp(ikz) \quad (2.1)$$

where k is the wavenumber and u the amplitude factor dependant of \mathbf{r} . Where \mathbf{r} describes the three-dimensional coordinate in space under the assumption that the vectorial character of light is uniform. However, a vectorial property of light such as the polarization undergoes a temporal change of directions, and therefore varies for different values of \mathbf{r} . This vector field in Cartesian coordinates with the x-axis and the y-axis expressed as the H-axis and V-axis respectively, is described by

$$\mathbf{u} = u_H \hat{H} + u_V \hat{V} \quad (2.2)$$

which can be used to separate the field $\mathbf{E}(z,t)$, which travels in the z-direction into the transverse components

$$e_H = u_H \cos \left[2\pi v \left(t - \frac{z}{c} \right) + \delta_x \right] \quad (2.3)$$

$$e_V = u_V \cos \left[2\pi v \left(t - \frac{z}{c} \right) + \delta_y \right] \quad (2.4)$$

for a plane wave. Equation (2.3) and ((2.4)) can be rewritten into the parametric equation of the ellipse

$$\frac{E_H^2}{u_H^2} + \frac{E_V^2}{u_V^2} - 2 \frac{E_H}{u_H} \frac{E_V}{u_V} \cos \delta = \sin^2 \delta \quad (2.5)$$

where $\delta = \delta_H - \delta_V$, describes the state of polarization (SOP) and E_H , E_V are the horizontal, respectively the vertical component of the $\mathbf{E}(z,t)$ field. The ellipse described by equation (2.5) has a major axis (\mathbf{f}) and a minor axis (\mathbf{s}), which depend on the polarization beam. This polarization ellipse can be described with help of two parameters, the orientation angle θ , and the ellipticity angle χ , defined as

$$\tan(2\theta) = \frac{2u_H u_V}{u_H^2 - u_V^2} \cos \delta, \quad 0 \leq \theta \leq \pi \quad (2.6)$$

$$\sin(2\chi) = \frac{2u_H u_V}{u_H^2 - u_V^2} \sin \delta, \quad -\pi/4 \leq \theta \leq \pi/4 \quad (2.7)$$

Introducing the proportionality parameter between the H- and the V- components, α such that

$$u_H = \cos \alpha \quad (2.8)$$

$$u_V = \sin \alpha \quad (2.9)$$

gives the opportunity to express the parameters purely trigonometrical [13]

$$\tan(2\theta) = \tan(2\alpha) \cos \delta \quad (2.10)$$

$$\sin(2\chi) = \sin(2\alpha) \sin \delta \quad (2.11)$$

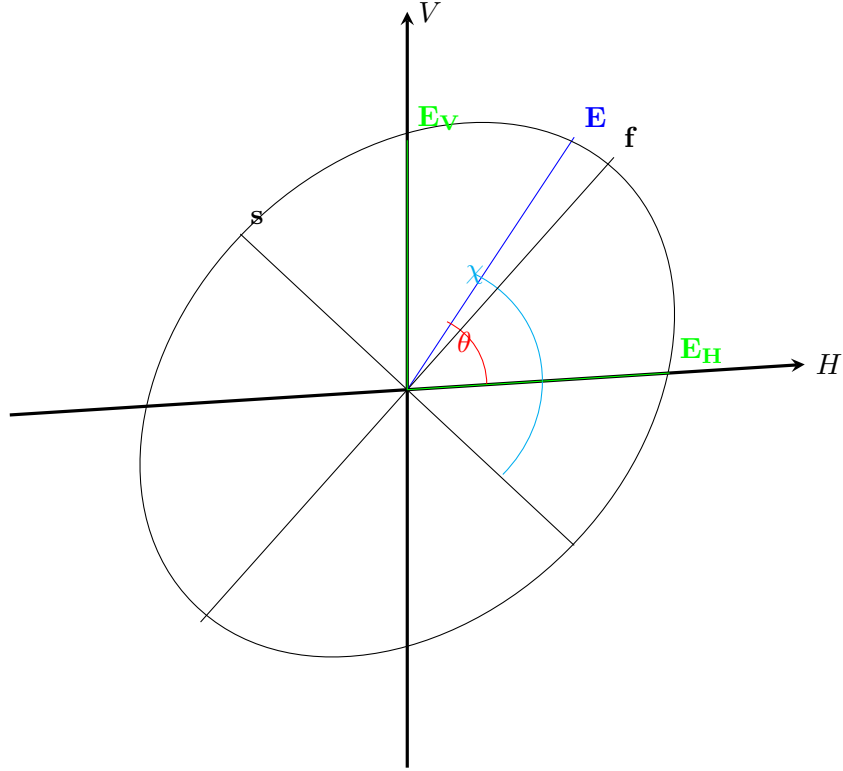


Fig. 2.1: polarization ellipse with the parameters describing the ellipse. χ is measured as the angle between the slow axis and the polarization vector, θ is the angle between the horizontal axis and the polarization vector.

Following from the ellipse equation (2.5) and the definitions of u_H and u_V , when $u_H = u_V$ for $\delta = \pm\pi/2$ **circular polarization state of polarization** (SOP) is created. Specifically when $\delta = \pi/2$ we observe right handed circular (R) light and when $\delta = -\pi/2$ left handed circular (L) light. If δ instead is 0 or π , it follows that the ellipse collapses to a straight line, where its slope depends on the ratio $\pm \frac{u_V}{u_H}$. The slope is horizontal (H), vertical (V), diagonal (D) or anti-diagonal (A) for $u_V = 0$, $u_H = 0$, $\frac{u_V}{u_H} = 1$ or $\frac{u_V}{u_H} = -1$ respectively.

An alternative description of the state of polarization (SOP) uses the **Stokes parameters**, which are

related to the amplitudes and the phase such as

$$\begin{aligned} S_0 &= u_H^2 + u_V^2 \\ S_1 &= u_H^2 - u_V^2 \\ S_2 &= 2u_H u_V \cos \delta \\ S_3 &= 2u_H u_V \sin \delta \end{aligned} \quad (2.12)$$

S_0 represents the intensity of the light and the parameters S_1 , S_2 , and S_3 correspond to the ratio of the amplitudes, the ellipticity, and orientation of the light field. For a fully polarised beam, the Stokes parameters can be considered as a real three-dimensional vector in Cartesian coordinates, which can be written to spherical coordinates:

$$\begin{bmatrix} S_1 \\ S_2 \\ S_3 \end{bmatrix} = S_0 \begin{bmatrix} \cos 2\chi \cos 2\theta \\ \cos 2\chi \sin 2\theta \\ \sin 2\chi \end{bmatrix} \quad (2.13)$$

Where the angles θ and χ are the same as the orientation angle and the ellipticity angle, respectively. The polarization state can now be pictured on the Poincaré sphere, as seen in figure 2.2. On this sphere, each point represents a specific SOP. The SOP on the north pole represents the R-SOP and the south pole the L-SOP, while the equator line represents various linear SOPs such as H, V, D and A. These states are related to each other via:

$$\hat{R} = \frac{1}{\sqrt{2}} (\hat{H} - i\hat{V}) \quad (2.14)$$

$$\hat{L} = \frac{1}{\sqrt{2}} (\hat{H} + i\hat{V}) \quad (2.15)$$

$$\hat{D} = \frac{1}{\sqrt{2}} (\hat{H} + \hat{V}) \quad (2.16)$$

$$\hat{A} = \frac{1}{\sqrt{2}} (\hat{H} - \hat{V}) \quad (2.17)$$

The points between the poles and the equator represent various elliptical states [14].

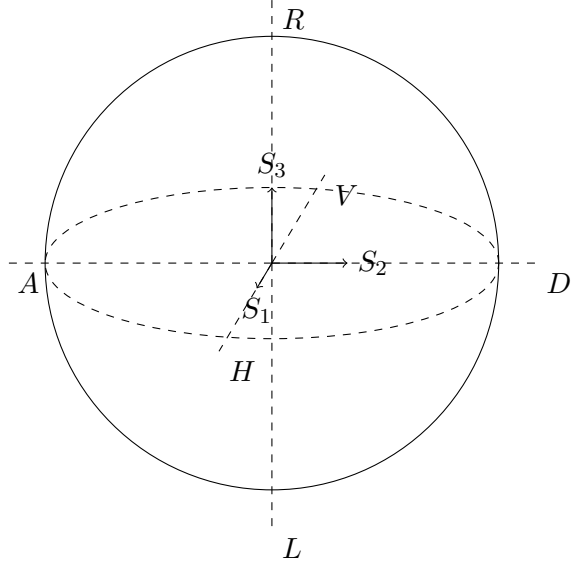


Fig. 2.2: The Poincaré sphere with the Stokes parameters visualised along the corresponding axis.

2.1.2 Polarization rotation

A light beam's SOP can be changed by, for example, an anisotropic crystal whose index of refraction is orientation dependent. This orientation dependency leads to a crystal with a so-called fast axis and a slow axis which in turn, introduces a phase shift between the light travelling along with the fast and the slow axis. The phase shift is also called retardation and is specified in units of degrees, waves, or nanometers. A full wave retardation is equivalent to 360° or the to a certain number of nanometers at a specific wavelength. If a polarization beam expressed in circular basis

$$\mathbf{E}_{\theta_0} = \frac{1}{\sqrt{2}} \left(e^{-i\theta_0} \mathbf{R} + e^{i\theta_0} \mathbf{L} \right) \quad (2.18)$$

propagates through an optically active material, inducing an additional phase difference of $2\Delta\theta$ between the right and left circularly polarised waves, then, the light beam will, after propagation through the phase shifting medium, have the form [15]

$$\mathbf{E}_{out} = \frac{1}{\sqrt{2}} \left(e^{-i\theta_0} e^{-i\Delta\theta} \mathbf{E}_R + e^{i\theta_0} e^{-i\Delta\theta} \mathbf{E}_L \right) = \cos(\theta_0 + \Delta\theta) \hat{x} + \sin(\theta_0 + \Delta\theta) \hat{y} \quad (2.19)$$

where the relationship between the wavelength λ and the retardation θ is

$$2\Delta\theta = \frac{\Delta n L 2\pi}{\lambda_0} \quad (2.20)$$

Knowing that $\frac{\Delta n}{\lambda_0} L = \frac{1}{2}$ for a HWP and for a QWP $\frac{\Delta n}{\lambda_0} L = \frac{1}{4}$ we can deduce the equation (2.20) for a half waveplate (HWP) and quarter waveplate (QWP) to:

$$2\Delta\theta = \pi \quad (2.21)$$

respectively:

$$2\Delta\theta = \frac{\pi}{2} \quad (2.22)$$

Therefore, the SOP of a light beam can be adjusted with the help of waveplates [16].

The above discussed phase shift is used for deterministic manipulate polarization rotation. Let a linear polarization be described by the polarization vector $\hat{\mathbf{p}}$, $\hat{\mathbf{f}}$ be the vector along the waveplates fast axis and $\hat{\mathbf{s}}$ the vector along the waveplates slow axis. The input light beam has the polarization

$$\mathbf{E}_{in} = E \left(\cos \theta \hat{\mathbf{f}} + \sin \theta \hat{\mathbf{s}} \right) \quad (2.23)$$

where θ denotes the angle between the polarization vector and the fast axis. When the beam travels through the half wave plate the phase shift in equation (2.21) is introduced. The effect of this term is $e^{i\pi} = -1$ between the fast and slow axis, and thus the output beam acquires the form

$$\mathbf{E}_{out} = E \left(\cos \theta \hat{\mathbf{f}} - \sin \theta \hat{\mathbf{s}} \right) = E \left(\cos (-\theta) \hat{\mathbf{f}} + \sin (-\theta) \hat{\mathbf{s}} \right) \quad (2.24)$$

This means that if the angular difference between the polarization propagation angle and $\hat{\mathbf{f}}$ is θ the polarization will be rotated by 2θ after the HWP. An example of this is seen in figure 2.3, where a horizontally polarised light beam propagates through a HWP with the fast axis aligned with the V-axis. The HWP induced retardation changes the polarization to vertical polarization.

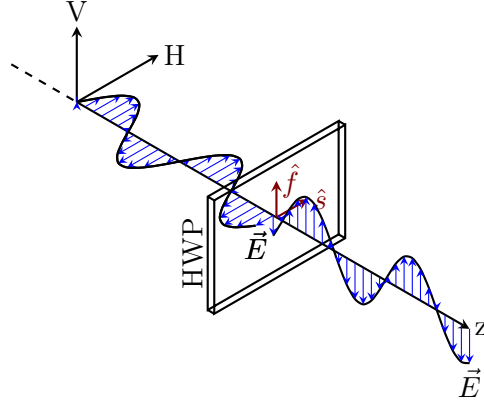


Fig. 2.3: Horizontally polarised light propagates through a HWP with the fast axis aligned with the V-axis.

If the light beam described by equation(2.23) instead propagates through a QWP, as seen in figure 2.4 the retardation index is $e^{i\frac{\pi}{2}} = i$ and the output beam is then described by

$$\mathbf{E}_{out} = E \left(\cos \theta \hat{\mathbf{f}} + i \sin \theta \hat{\mathbf{s}} \right) \quad (2.25)$$

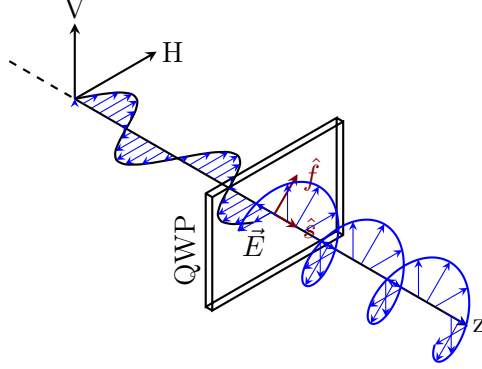


Fig. 2.4: Horizontal polarised light propagates through a QWP with the fast axis aligned with the V-axis.

In the same manner, if the input SOP is elliptical polarised, the trip through a QWP will produce a linear output SOP.

Retardation induced by a waveplate can be described by the Jones matrix. A general waveplate induces a retardation δ such that

$$\mathbf{J}_{WP} = \begin{bmatrix} e^{i\delta} & 0 \\ 0 & e^{-i\delta} \end{bmatrix} \quad (2.26)$$

For a half wave plate and a quarter wave plate the retardation is described by

$$\mathbf{J}_{HWP} = \begin{bmatrix} 1 & 0 \\ 0 & -1 \end{bmatrix} \quad (2.27)$$

and

$$\mathbf{J}_{QWP} = \begin{bmatrix} 1 & 0 \\ 0 & -i \end{bmatrix} \quad (2.28)$$

respectively. However, these matrices consider only the case when the fast axis is along the horizontal axis and the slow axis along the vertical axis. But if the fast axis is tilted by an arbitrary angle θ with respect to the horizontal axis, the rotation matrix is

$$\mathbf{R}(\theta) = \begin{bmatrix} \cos \theta & \sin \theta \\ -\sin \theta & \cos \theta \end{bmatrix} \quad (2.29)$$

and the matrix for the waveplate is described by

$$\mathbf{J}(\theta) = \mathbf{R}(-\theta) \mathbf{J}_{WP} \mathbf{R}(\theta) \quad (2.30)$$

By substituting the terms in 2.30 the matrix describing the HWP then becomes

$$\mathbf{J}_{HWP}(\theta) = \begin{bmatrix} \cos(2\theta) & \sin(2\theta) \\ \sin(2\theta) & -\cos(2\theta) \end{bmatrix} \quad (2.31)$$

and the matrix describing the QWP becomes [13]

$$\mathbf{J}_{QWP}(\theta) = \begin{bmatrix} \cos^2 \theta - i \sin^2 \theta & (1-i) \cos \theta \sin \theta \\ (1-i) \cos \theta \sin \theta & \sin^2 \theta + i \cos^2 \theta \end{bmatrix} \quad (2.32)$$

2.1.3 Polarization transform to an arbitrary state of Plarization

It has been proved that an SOP can be transformed to any point on the Poincaré sphere with two QWPs and one HWP in arbitrary order [17]. Since every waveplate has one degree of freedom, the system of waveplates has three degrees of freedom. However, Heisman [18] showed that the system could be reduced to a two degree of freedom system defined as

$$\text{Rotation of QWP1} = \frac{\beta}{2} \quad (2.33)$$

$$\text{Rotation of QWP2} = \frac{\beta}{2} + \frac{\varepsilon}{2} \quad (2.34)$$

$$\text{Rotation of HWP} = \frac{\gamma}{2} \quad (2.35)$$

where ε has a constant value. This constant has been proven to be able to be fixated at $\varepsilon = \pi$ and reaching every SOP on the Poincaré sphere [19]. The Jones matrices corresponding to the rotation operations performed by waveplates such as seen in equations (2.21) - (2.33) on a input SOP are

$$\mathbf{J}_{QWP1}\left(\frac{\beta}{2}\right) = \begin{bmatrix} \cos^2\left(\frac{\beta}{2}\right) - i \sin^2\left(\frac{\beta}{2}\right) & (1-i)\cos\left(\frac{\beta}{2}\right) \\ (1-i)\cos\left(\frac{\beta}{2}\right) & \sin^2\left(\frac{\beta}{2}\right) + i \cos^2\left(\frac{\beta}{2}\right) \end{bmatrix} \quad (2.36)$$

respective

$$\mathbf{J}_{HWP}\left(\frac{\gamma}{2}\right) = \begin{bmatrix} \cos(\gamma) & \sin(\gamma) \\ \sin \gamma & -\cos \gamma \end{bmatrix} \quad (2.37)$$

and

$$\mathbf{J}_{QWP2}\left(\frac{\beta}{2} + \frac{\varepsilon}{2}\right) = \begin{bmatrix} \cos^2\left(\frac{\beta}{2} + \frac{\varepsilon}{2}\right) - i \sin^2\left(\frac{\beta}{2} + \frac{\varepsilon}{2}\right) & (1-i)\cos\left(\frac{\beta}{2} + \frac{\varepsilon}{2}\right) \\ (1-i)\cos\left(\frac{\beta}{2} + \frac{\varepsilon}{2}\right) & \sin^2\left(\frac{\beta}{2} + \frac{\varepsilon}{2}\right) + i \cos^2\left(\frac{\beta}{2} + \frac{\varepsilon}{2}\right) \end{bmatrix} \quad (2.38)$$

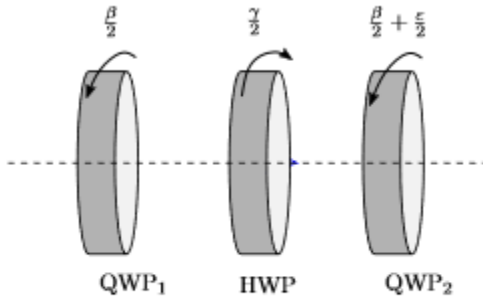


Fig. 2.5: Schematic diagram of the polarization transforming system.

If these waveplates are placed in a cascade, as seen in figure 2.5, the transformation matrix becomes

$$\mathbf{T} = \mathbf{J}_{QWP2}(\beta/2 + \varepsilon/2) \cdot \mathbf{J}_{HWP}\left(\frac{\gamma}{2}\right) \cdot \mathbf{J}_{QWP1}(\beta/2) \quad (2.39)$$

where the total output SOP can then be calculated by

$$\mathbf{E}_{out} = \mathbf{T} \cdot \mathbf{E}_{in} \quad (2.40)$$

where \mathbf{T} is the transmission matrix defined in equation (2.39), and \mathbf{E}_{in} the input SOP.

2.1.4 Polarization control

Due to the non-linearity of polarization drift induced in fibre a PID-controller (proportional–integral–derivative controller) is not suitable for control of the polarization drift [20]. Therefore are other approaches required for successful polarization control. However, if a system for polarization drift correction to a predefined SOP only relies on polarization rotation based on the method discussed in section 2.1.2, then the system will be unstable. Because by only relying on a polarization rotating system, it allows the polarization to drift randomly within a certain interval before it is corrected. Therefore, a stabilization algorithm is a useful method for stabilization of a random polarization drift.

Polarization has been successfully stabilised with various stabilisation methods. One of these methods is the gradient method, which uses the gradient to find the goal state. Although this is an efficient algorithm for polarization stabilisation, it requires knowledge of the input SOP, directly or by reconstruction [21]. To reconstruct the input SOP equation (2.40) can be used since

$$\mathbf{E}_{in} = \mathbf{T}^{-1} \cdot \mathbf{E}_{out} \quad (2.41)$$

However, the use of equation (2.41) requires ideal WPs, or the transformation matrix must be calibrated for the imperfections.

Using a flexible optimisation algorithm is an option when neither direct knowledge of the input SOP nor perfect reconstruction of the input SOP from the output SOP and the transmission matrix is possible. One of these flexible optimisation algorithms is the particle swarming optimisation (PSO) algorithm. This algorithm has previously been successfully implemented for polarization stabilisation [22]. The PSO-algorithm optimises the problem by an iterative stochastic method where multiple solutions are tested for minimisation of the function. The algorithm starts with initiating a population (swarm) of possible solutions (particles). These particles are moved around in the search-space according to a few simple formulas. The movements of the particles are guided by their own best known position in the search-space as well as the entire swarms best known position. When improved positions are being discovered these will then come to guide the movements of the swarm. The process is repeated until a satisfying solution is found. In this algorithm every particle is defined by its position x_i and its velocity v_i

$$v_i^{t+1} = \omega v_i^t + c_1 r_1 x_{Best_i} - x_i^t + c_2 r_2 g_{Best_i} - x_i^t \quad (2.42)$$

$$x_i^{t+1} = x_i^t + v_i^t \cdot t \quad (2.43)$$

where x_{Best} is the particles best position and g_{Best} is the entire groups best position. ω is the inertia weight, c_1 and c_2 two position constants, and r_1 and r_2 two random parameters within $[0,1]$ [23]. The efficiency of this algorithm is then dependent on the function of minimisation.

Chapter 3

Method

3.1 The fibre link

The dark fibre link is provided by Stokab and it consists of 8km of standard single mode fibre (SSMF28) that runs from the Quantum Nano Photonics (QNP) lab at Albanova University Center in Stockholm City to the Ericsson lab in Kista. This fibre link is originally made for classical telecom communication and is, therefore, a non-polarization maintaining optical fibre optimised for telecom wavelength. However, for reducing the power loss are the fibre couplings spliced at all possible connections, which reduces the loss to 10.8 dB.

3.2 Setup components

3.2.1 Polarimeter



(a) Pax1000 polarimeter is used in Ericsson lab.
Image source [24]



(b) PAX5710 Polarimeter is used in the QNP lab.
Image source [25]

Fig. 3.1: The polarimeters used for polarization measurements.

Polarimeters are used to measure a light beams SOP, during our measurements have two polarimeters been used. In Ericsson lab is the polarization measured with Thorlabs PAX1000 polarimeter seen in figure 3.1a, which measures the polarization within a wavelength from 900-1700 nm with $\pm 0.25^\circ$ accuracy for the azimuth- and ellipticity angle. The polarimeter can be used in a free space optics configuration or fibre coupled. To this end, a lens tube with a fibre collimator is provided. The other polarimeter model are used in QNP lab, where a PAX5710 Polarimeter has been used. This polarimeter is also designed for free space measurements, but a removable collimation package also allows fibre measurements. This unit is the black box seen in figure 3.1b and is attached to the polarimeter, which is the grey box seen in figure 3.1b. The accuracy of this polarimeter is $\pm 0.2^\circ$ for the azimuth- and ellipticity angle.

Both polarimeters use the relationship between the light intensity measured in different basis to estimate the SOP. The SOP can be constructed from the Stokes parameters in equation (2.13) and it corresponds to a state on the surface of a Poincaré sphere with radius S_0 . The component along the RL-axis is then S_3

$$S_3 = \cos(2\chi) = \cos^2 \chi - \sin^2 \chi = \frac{I_R - I_L}{I_0} \quad (3.1)$$

where I_R and I_L are the intensities of the light in the R respectively L SOPs such as

$$I_0 = I_R + I_L = I_H + I_V = I_D + I_A \quad (3.2)$$

Where I_0 is the total intensity, I_H , I_V , I_D and I_A are the intensities in the H-, V-, D-, A-basis, respectively. It can now be shown that S_1 expressed with relationship to the HV-polar axis coordinates is

$$S_1 = \cos(2\alpha) = \cos^2 \alpha - \sin^2 \alpha = \frac{I_H - I_V}{I_0} \quad (3.3)$$

and if the proportionality parameter between the A- and D- components is ζ [26], then

$$S_2 = \cos(2\zeta) = \cos^2 \zeta - \sin^2 \zeta = \frac{I_D - I_A}{I_0} \quad (3.4)$$

To perform the measurements, both polarimeters use a technique based on a rotating QWP, a linear polariser, and a photodiode. The QWP is automatically rotated by a DC-motor, and can therefore modulate the polarization of the incoming lightbeam. The light is then filtered by the polariser and it impinges on the photodiode. The light intensity is then used to calculate the Stokes parameters with equations (3.1)- (3.4) [24]. The only difference between the polarimeters are that PAX5710 has an external measurement sensor, the grey box seen in figure 3.1b, while PAX1000s' sensor is built-in.

3.2.2 Polarization controller

The polarization controlling system is based on two QWPs and one HWP. These WPs are from B.Halle, and made in quarts and MgF₂. The HWP has a deviation of retardation specified to $\pm 0.04\%$ and a variation of the axis direction of $\pm 0.2\%$, and the QWPs deviation are specified to $\pm 0.025\%$ and the variation of the axis direction to $\pm 0.1\%$. These WPs are mounted on a PI (Physik Instrumente)-stage with 2-phase stepper motors each. The PI-stages are controlled by a Mercury C-662.11 step motor, from Physik Instrumente. The PI-stages rotate the WPs based on the desired angle measured in relation to a fixed reference axis. The step motors are controlled with Python and Physics instruments Python package PIPython.

3.2.3 Light filtering

The control signal and the signal of interest is differentiated with BragGrateTM Notch Filter. This filter differentiates light based on their wavelength on a very narrow bandwidth, here at a bandwidth of 0.7 nm, at a wavelength of 1550 nm. The light at the right wavelength passes through, and other wavelengths are reflected.

3.3 Setups

In this work we have used three different setups to be able to measure the polarization drift, to characterise the waveplates and to control the polarization.

3.3.1 Polarization drift measurement

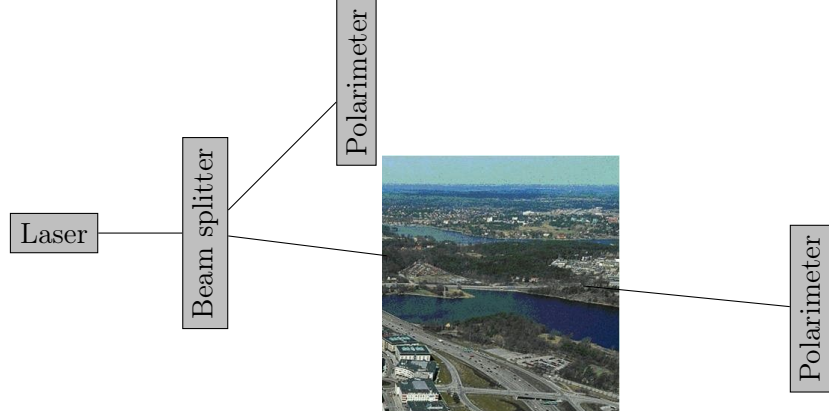


Fig. 3.2: The setup used for measurement of the uncontrolled polarization drift. The laser in QNP lab launches a light beam into a fibre, this light beam is then splitted by a beamsplitter. The weak arm of the splitted light beam ins leads to the PAX5710 Polarimeter at the QNP lab. The strong arm is lead though the fibre link to Ericsson lab. The light beams SOP is measured with the PAX1000 polarimeter in the Ericsson lab.

Image source [1]

The investigation of the polarization drift over the fibre link requires measurements with two polarimeters, one at the light source in the KTH lab and one in the Ericsson lab. As seen in figure 3.2, the light beam is generated with a laser in the QNP lab, at a power of ~ 30 mW (ca 15 dBm) and with a defined polarization. The light beam is split with a 9/1 non-polarising in-fibre beam splitter. The weaker beam (10% of the light) is led to the PAX5710 Polarimeter in QNP which records the SOP, and the strong beam (90%) is led through the link to Ericsson lab. At the end, the optical fibre directly coupled to the PAX1000 polarimeter, which records the SOP with 30 s intervals.

3.3.2 Waveplate characterisation

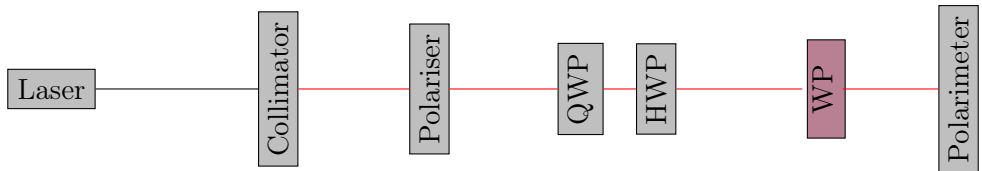


Fig. 3.3: Setup used for characterisation of the waveplates. Blue link indicates a fibre link, red links indicate FSO (free space optical) link. After collimating the laser light, the beam propagates through a polariser, one QWP and one HWP. Thereafter propagates the light beam through the WP of interest for characterisation before the polarization is measured by the polarimeter.

The characterisation of the waveplates is performed with a local laser, a fibre collimator, a polariser, one quarter waveplate, one half waveplate and the PAX1000 polarimeter. The laser launches a light beam with a power of ~ 3.9 mW (ca 6dBm) into an optical fibre, which leads the light beam to the collimator. The light beam is then filtered with a polariser to make sure the degree of polarization is 100 %, and does not drift. The remaining light beam can then be changed to any pure SOP by the QWP and the HWP. Here, they are used to set the SOP to the H-, V-, R-, and L-states. After the SOP controlling WPs, we place the WP of interest for characterisation. This WP is then

rotated in steps of 0.5° , at each step the SOP is recorded by the polarimeter.

3.3.3 Initial setup for polarization control

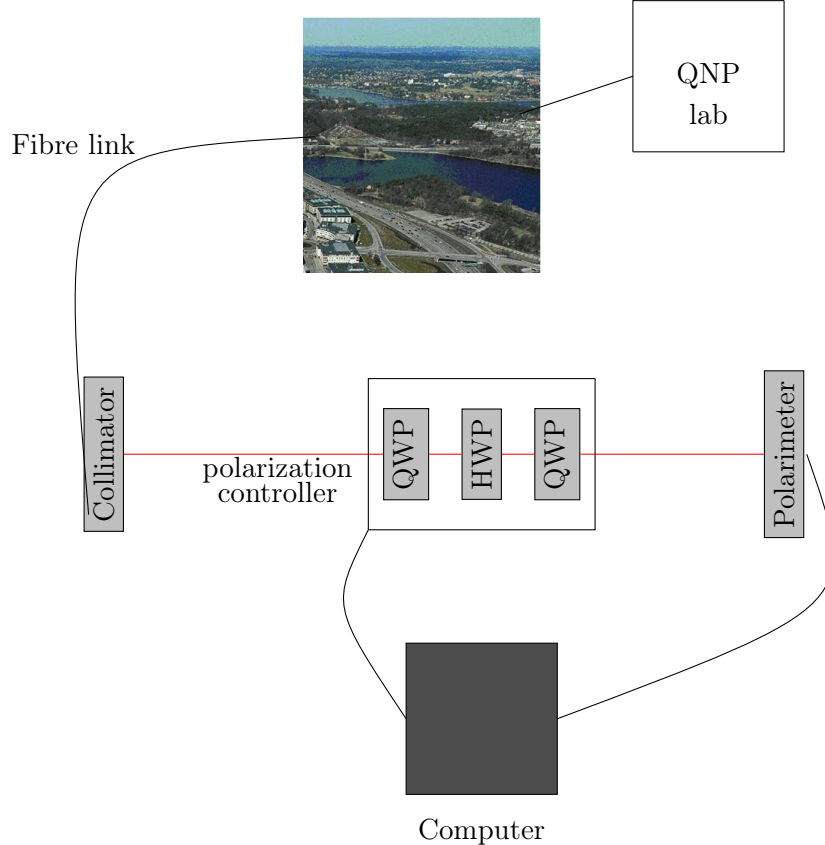


Fig. 3.4: Initial setup used for polarization control. Grey links identify fibre based connections and red links are used for FSO. A laser in the QNP lab launches the lightbeam into the optical fibre. The light beam propagates through the fibre link to the Ericsson lab. There the collimator will launch the light into the FSO link. Thereafter, the light beam propagates through the polarization controller, which can change the SOP. Finally, the SOP is measured by the polarimeter.

Image source [1]

In the setup focusing on polarization control, the free space optics components are aligned along a line as seen on figure 3.4. In this setup the lightbeam is launched from the QNP laboratory with a power of ~ 30 mW into an optical fibre connected to the link. Once at Ericsson the lightbeam is then launched into free space optics by the collimator. The lightbeam propagates then through the polarization controller to the PAX1000 polarimeter, which records the data. The collected SOP data is used for calculating the required rotation of the waveplates with the PSO-algorithm, which is performed by a computer connected to the polarimeter. The optimal angles between the fast axis of each WP and the labs horizontal axis are then used to rotate the WPs in the polarization controlling setup.

3.3.4 Final setup for polarization control in Ericsson lab

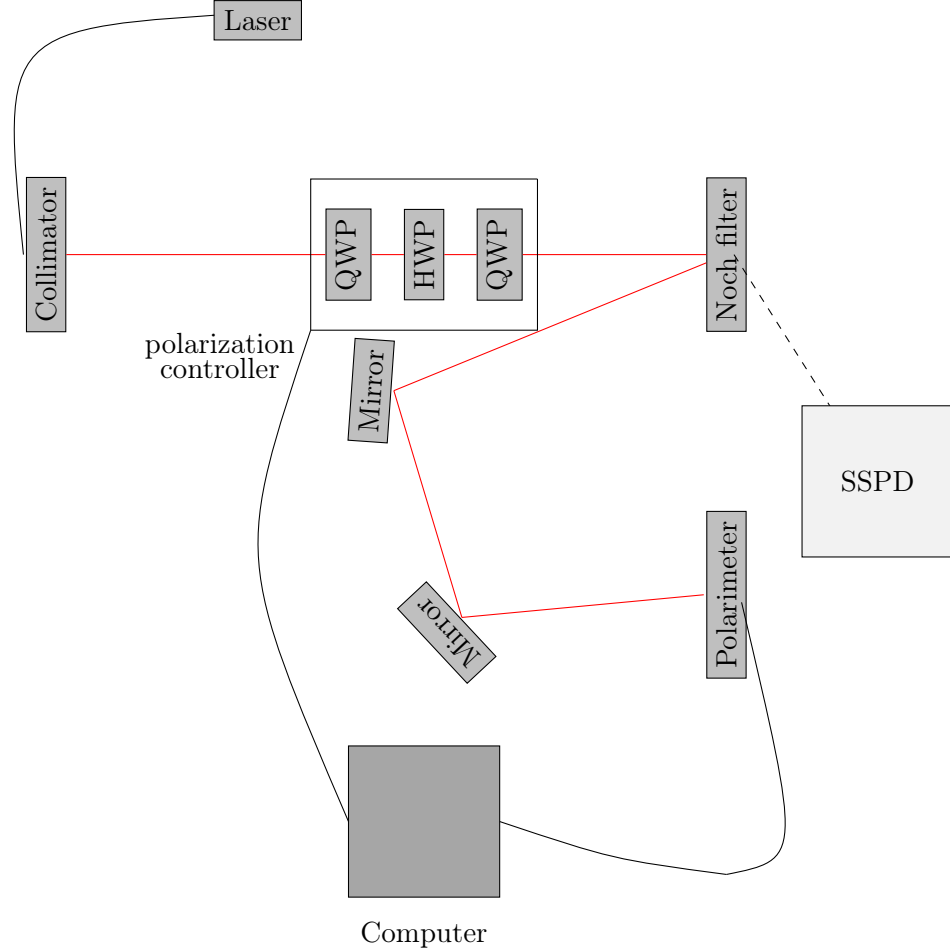


Fig. 3.5: The final setup, which allows the polarization control to be combined with single photon counting technology. Here paired with a local laser.

The final setup is prepared for measurements of single photons. The first part of the setup is identical to the setup seen in figure 3.4. However, after the polarization controller, the polarimeter is replaced with a notch filter. This notch filter filters the control signal but lets the single photons passing through. The reflected control signal is then reflected by two mirrors before it arrives at the polarimeter. This final setup is here pictured with the collimator connected to the local laser since the only measurements performed with this setup used the local laser. However, this setup is intended to be used with the fibre link connecting QNP lab and Ericsson lab.

3.4 polarization controlling algorithm

The polarization control is based on the PSO-algorithm, and the minimisation function on

$$f_{min} = \left| \left(S_1^{goal} - S_1^{out}, S_2^{goal} - S_2^{out}, S_3^{goal} - S_3^{out} \right) \right| \quad (3.5)$$

where the S-parameters are the Stoke parameters corresponding to the index.

The output SOP depends on the input SOP and the rotation angles of the WPs. The output SOP used in the analytical calculations for equation (3.5) is constructed via the input SOP, which is measured when the WPs fast axes are aligned with the horizontal axis such that

$$\mathbf{T} = \mathbf{I} \quad (3.6)$$

Where the transmission matrix is the matrix for an ideal series of two QWPs and one HWP. the state \mathbf{S}^{out} can then be described as

$$\mathbf{S}^{out} = \mathbf{T}\mathbf{S}^{in} \quad (3.7)$$

Where \mathbf{T} is the transfer matrix defined in equation (2.39). The results of the minimisation of equation 3.5 are then used to rotate the WPs in the polarization controlling setup, and for simulating the results with theoretical, ideal WPs. The results from the rotation of the real WPs and the ideal WPs can then be compared. The error limit is set such that, the algorithm searches for the best rotation values until $f_{min} \leq 0.1\%$. The algorithm is active as long as the relative error between the measured output SOP and the theoretical output SOP is below 25 %. This limit is decided after a series of empirical tests of which level of precision is possible to reach repeatedly for various SOPs entering the polarization controllers, and various goal SOPs, and also be of a meaningful precision level.

3.5 Error calculations

The relative error can be calculated according to

$$\text{Error} = \frac{|\mathbf{S}_{measured} - \mathbf{S}_{theoretical}|}{|\mathbf{S}_{theoretical}|} \times 100 \quad (3.8)$$

where $\mathbf{S} = [S_0, S_1, S_2, S_3]$ and $S_0^{measured} = S_0^{theoretical}$. Equation 3.8 estimates the relative difference between the output achieved with ideal WPs and the real WPs. In our setup, an error of 100 % would therefore mean that the measured output SOP is at one of the eight possible mirroring states to the theoretical output SOP. Mirroring states are states on an other of the identical eightths a sphere can be divided in.

Chapter 4

Results and discussion

4.0.1 Polarization drift measurements

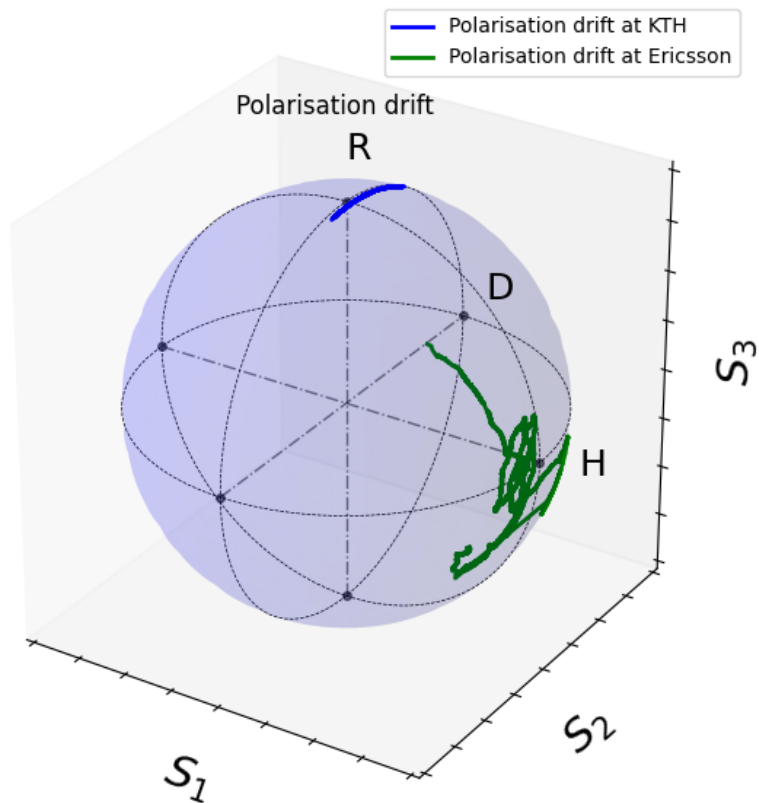
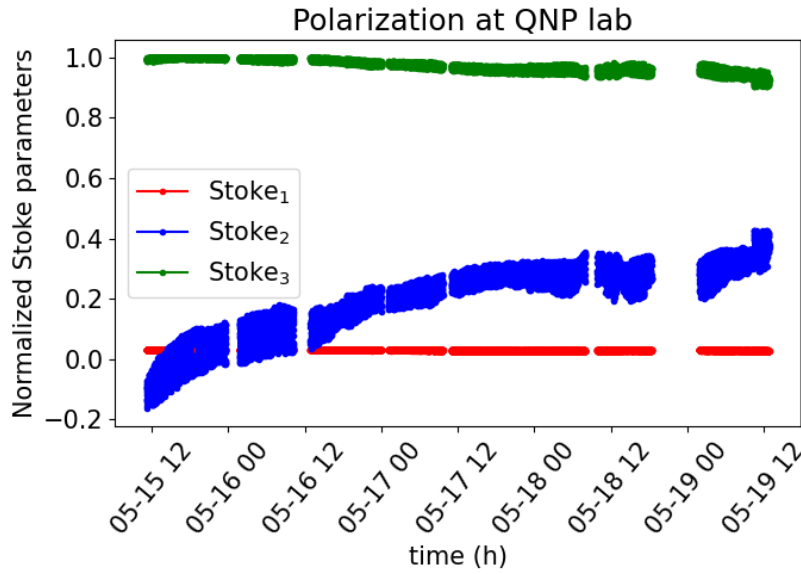


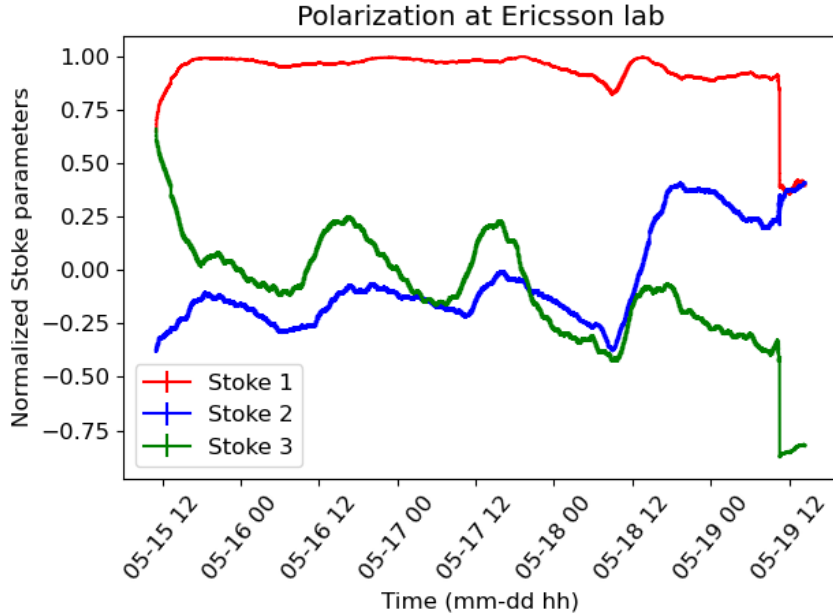
Fig. 4.1: The polarization drift at QNP lab and Ericsson labs, measured during 15-19 May 2020. The **stoke vectors** are normalised for visualisation of the polarization on the **Poincaré sphere**.

The polarization drift in the fibre link between QNP lab and Ericsson lab was measured during May 15-19th, 2020. The **SOPs** measured during this period are seen in figure 4.1, where it can be seen that the **ellipticity** of the polarization at QNP lab **slowly drifts**. This drift could be due to the **non-polarization maintaining beamsplitter** used to divide the light beam between the light sent to

Ericsson and the recording of the SOP at the QNP lab. It can also be seen that the polarization has rotated approximately 90° when it arrives at the Ericsson lab. Although a polarization drift is induced by the fibre link, the drift, as seen in figure 4.1 is slow, with an average change of $0.759\% \pm 0.409\%$ and centred at one side of the Poincaré sphere. This means that the time factor is not a critical element for the polarization controlling algorithm.



(a) The polarization measured in QNP lab with the PAX5710 Polarimeter. The breaks in the graphs stem from breaks in the measurements due to the operation of the PAX5710.



(b) The polarization measured at Ericsson lab with PAX1000 Polarimeter.

Fig. 4.2: polarization drift, measured 15-19 May 2020. the polarization at QNP in (a) and the drift of the polarization after travelling through the fibre link in (b). The normalised Stokes parameters are individually plotted against the time at the x-axis. This enables easy visualisation of the chronology of the polarization drift induced by environmental variations which impact the fibre link.

Figure 4.2 shows the separate Stokes parameters, S_1, S_2, S_3 , plotted versus time. It can be seen that the polarization at QNP lab is reasonably stable, while the polarization drifts at Ericsson lab. Nonetheless, the polarization drift measured at Ericsson lab is slow except a drastic change on 19 May at 12:00. This dramatic change of the polarization was because of a person touching the fibre in the QNP lab. It can, therefore, be concluded that the polarization is sensitive to changes already in the QNP lab. And even if the polarization usually changes slowly, fast changes can occur.

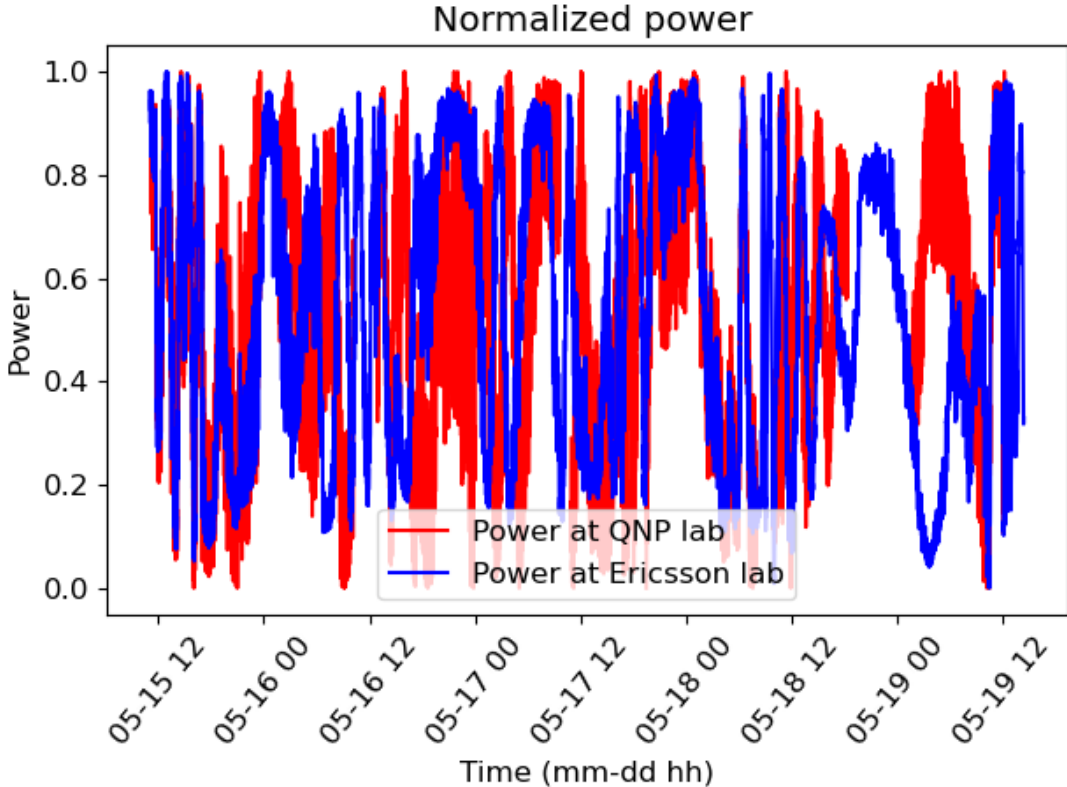


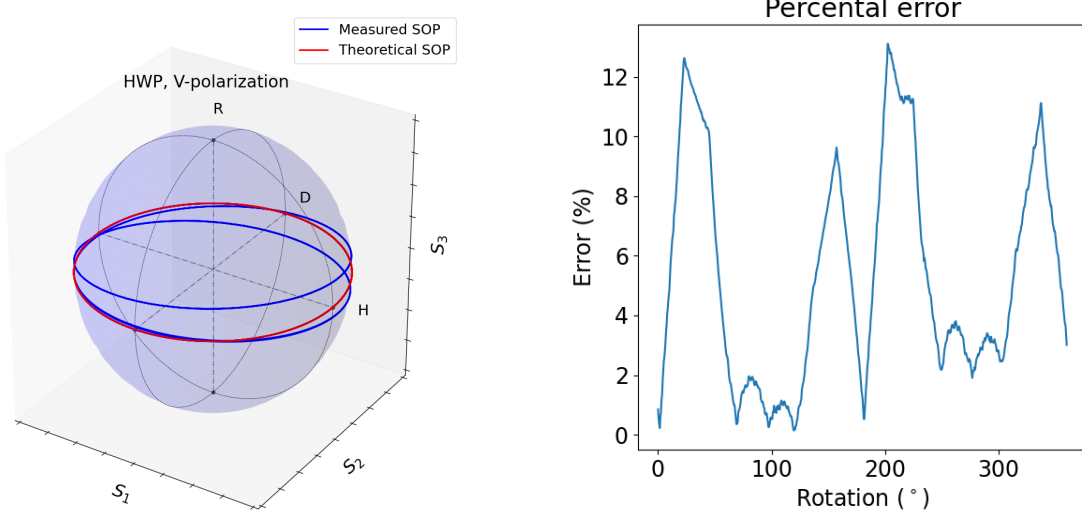
Fig. 4.3: The power drift at QNP lab and Ericsson lab during the polarization drift measurement 15-19 May 2020, normalised with the min-max feature scaling. The y-axis shows the normalised power, and the x-axis the time.

Figure 4.3 shows the normalised power drift at the QNP and Ericsson labs. The power is normalised with min-max feature scaling. Studying the normalised power in figure 4.3, we observe that the power fluctuation seems to have the same shape in QNP lab and Ericsson lab. This implies that the power loss through the propagation in the fibre is equally distributed. This implies that all polarization is equally sensitive to power loss.

4.1 Waveplate characterisation

The final performance of the algorithm that will stabilise the polarization of the link is directly related to the performance and reliability of the individual optical components used. In our set up the waveplates are mounted on optical mounts and are rotated thanks to the PI-stages. All these factors have a non-zero intrinsic error that we need to characterise.

4.1.1 Characterisation of HWP

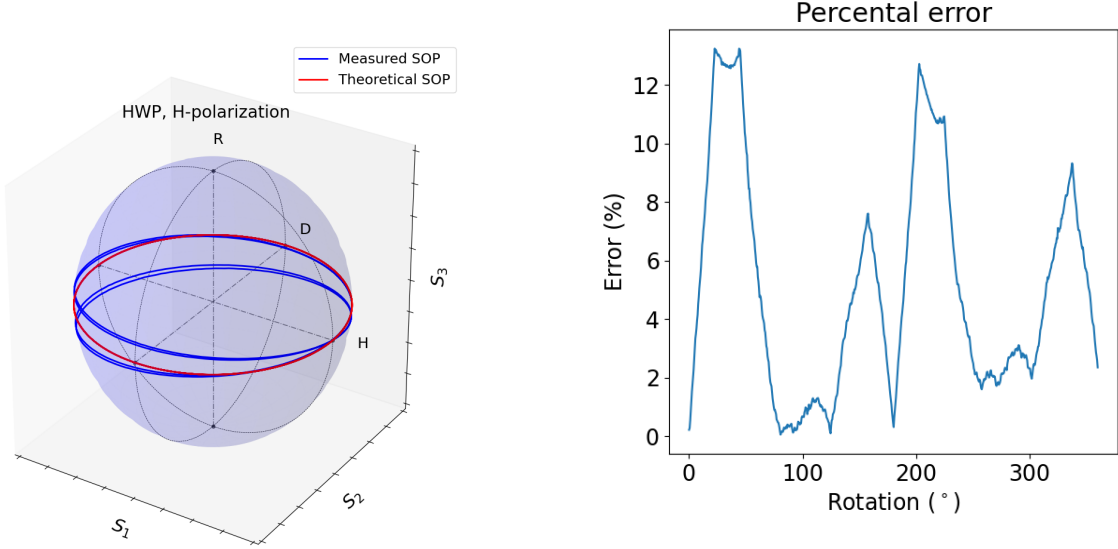


(a) The output SOP from the ideal HWP and the real HWP visualised on the Poincaré sphere.

(b) The percental between the theoretical output SOP and the measured output SOP plotted versus the rotation angle of the HWPs rotation versus the fast axis.

Fig. 4.4: Characterisation of the HWP, where the input SOP has the V-state. The measured output SOP is compared with the output SOP produced by an ideal HWP.

By studying figure 4.4b it can be noticed that for the used HWP, with a V-polarised input SOP, the relative error is as high as $13.0107\% \pm 0.162\%$. As seen in the visualisation of the SOPs on the Poincaré sphere in figure 4.4a, this error is mainly due to elliptical polarization induced by the HWP. This induced ellipticity is due to the imperfection of the HWP.

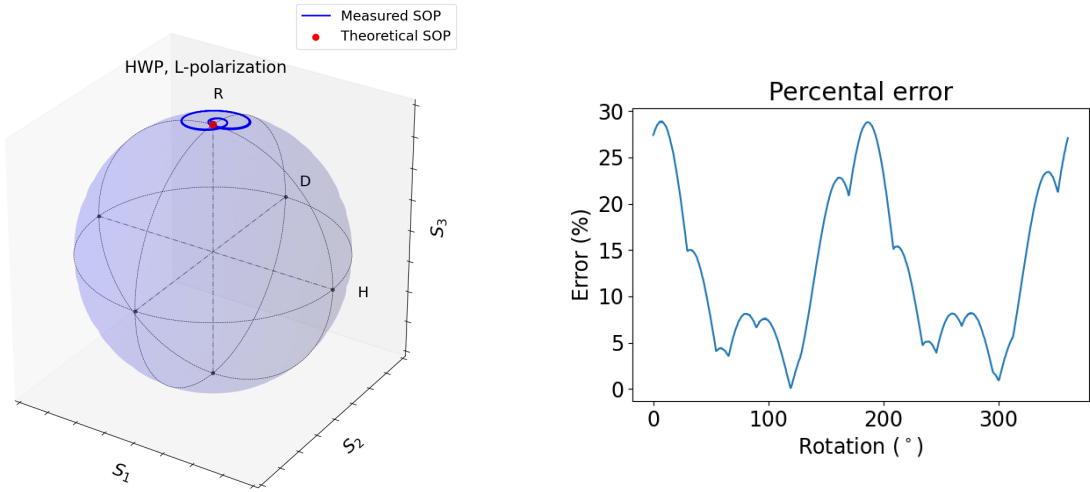


(a) The output SOP from the ideal HWP and the real HWP visualised on the Poincaré sphere.

(b) The relative error in percent between the theoretical output SOP and the measured output SOP plotted versus the rotation angle of the HWPs rotation versus the fast axis.

Fig. 4.5: Characterisation of the HWP, where the input SOP has the H-state. The measured output SOP is compared with the output SOP produced by an ideal HWP.

A similar difference between the measured SOP and the theoretical SOP is observed for an input SOP in the H-state as for an input SOP in the V-state. Figure 4.5b shows a similar error profile as seen in figure 4.4b. But figure 4.5a shows that the difference between the theoretical SOP and the measured SOP is at a maximum when the rotated SOP is at V. As opposed to the plot in figure 4.4a where the maximum error of $13.247\% \pm 1.101\%$ is observed for the H-state. From these results can it be concluded that the maximum difference between the theoretical predicted output SOP and the measured SOP is the SOP on the opposite side of the Poincaré sphere to the input SOP.

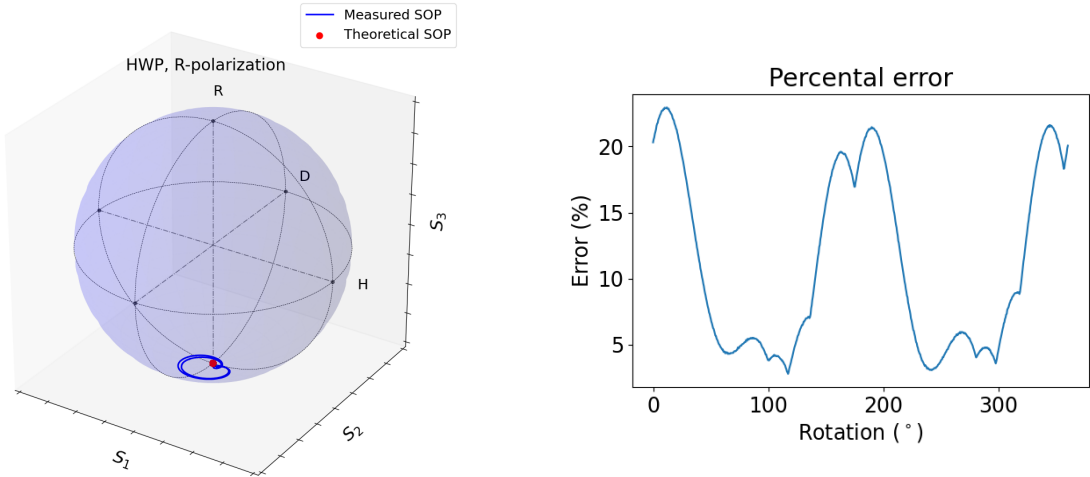


(a) The output SOP from the ideal HWP and the real HWP visualised on the Poincaré sphere.

(b) The relative error in percent between the theoretical output SOP and the measured output SOP plotted versus the rotation angle of the HWPs rotation versus the fast axis.

Fig. 4.6: Characterisation of the HWP, where the input SOP has the L-state. The measured output SOP is compared with the output SOP produced by an ideal HWP.

As seen in figure 4.6a, the HWP clearly influences the the ellipticity of the SOP during the rotation of the HWP. This is in opposition to the theoretical SOP, which is seen by the single point point at the south pole This reflects the relative error, which as seen in figure 4.6b can be as high as $28.889\% \pm 0.519\%$.



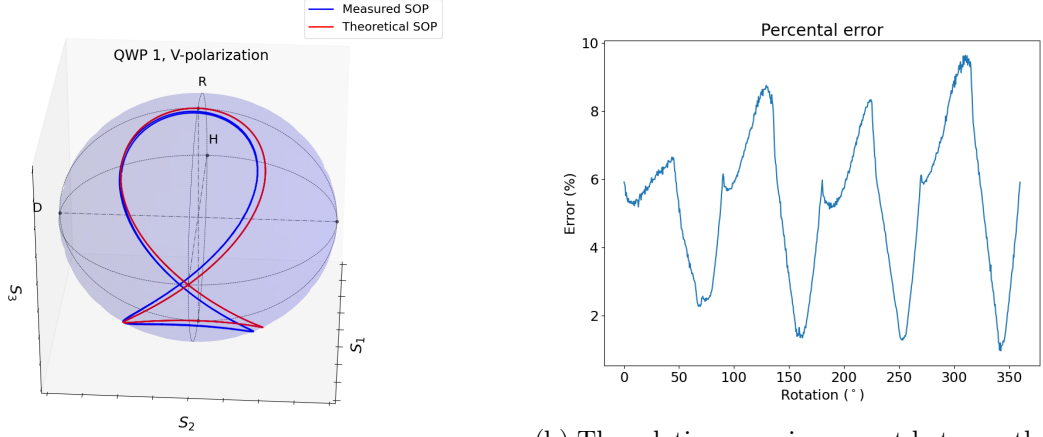
(a) The output SOP from the ideal HWP and the real HWP visualised on the Poincaré sphere.

(b) The relative error in percent between the theoretical output SOP and the measured output SOP plotted versus the rotation angle of the HWPs rotation versus the fast axis.

Fig. 4.7: Characterisation of the HWP, where the input SOP has the R-state. The measured output SOP is compared with the output SOP produced by an ideal HWP.

Figure 4.7 is analogue to Figure 4.6 but with an R input polarization state. As it can be seen figure 4.7a shows how the HWP influences the the ellipticity of the SOP during the rotation of the HWP. The main difference is that the SOP, which is centred around the north pole at the sphere instead of the south pole. This is also reflected in the relative error, which as seen in figure 4.7b can be as high as $22.959\% \pm 0.450\%$, a relative error in the same order as the relative error for the L-state.

4.1.2 Characterisation of quarter waveplate 1

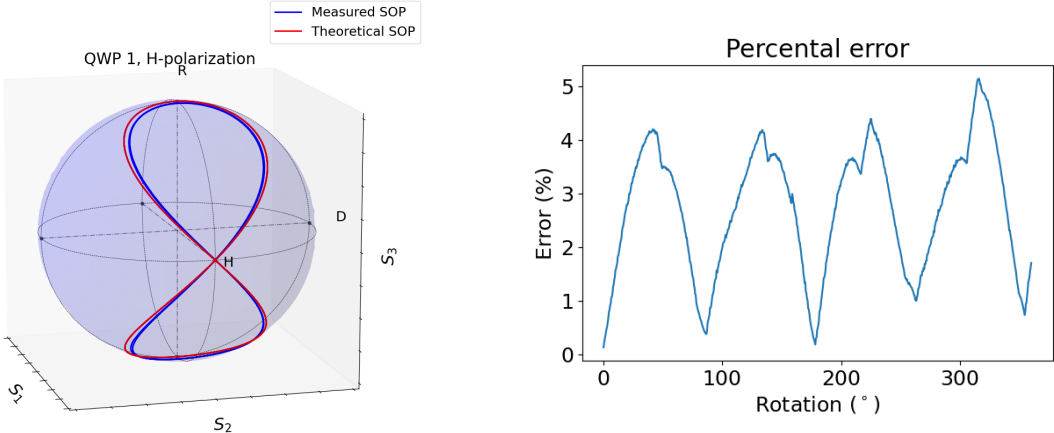


(a) The output SOP from the ideal QWP and the real QWP 1 visualised on the Poincaré sphere.

(b) The relative error in percent between the theoretical output SOP and the measured output SOP plotted versus the rotation angle of the QWP 1's rotation of the fast axis versus the horizontal axis.

Fig. 4.8: Characterisation of the QWP 1, where the input SOP has the V-state. The measured output SOP is compared with the output SOP produced by an ideal QWP.

Figure 4.8a shows that the output SOP produced by the QWP 1 from a V-polarised input SOP roughly follows the theoretical predicted output SOP. But how close the real curve follows the theoretical curve varies for different SOPs. It is seen in figure 4.8b that the maximal difference is $9.627\% \pm 0.839\%$.

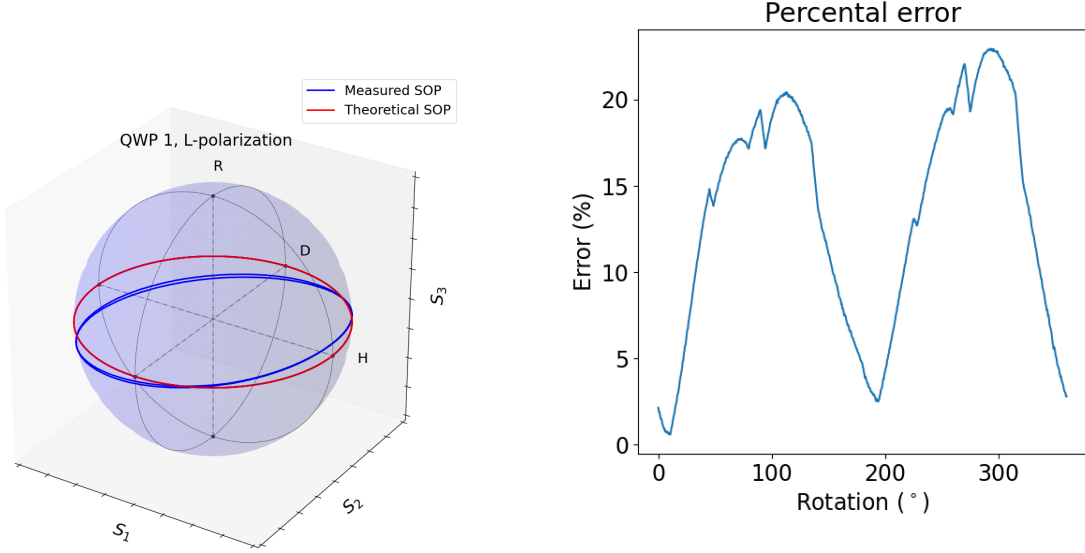


(a) The output SOP from the ideal QWP and the real QWP 1 visualised on the Poincaré sphere.

(b) The relative error in percent between the theoretical output SOP and the measured output SOP plotted versus the rotation angle of the QWP 1's rotation of the fast axis versus the horizontal axis.

Fig. 4.9: Characterisation of the QWP 1, where the input SOP has the H-state. The measured output SOP is compared with the output SOP produced by an ideal QWP.

Figure 4.9a shows that the output SOP produced by the QWP 1 from a L-polarised input SOP diverges from the theoretical output SOP. This divergence has its maximum at the surroundings of the vertical state on the Poincaré sphere. It is seen in figure 4.9b that the maximal relative error is $5.153\% \pm 0.649\%$, which is the smallest observed maximal relative error.

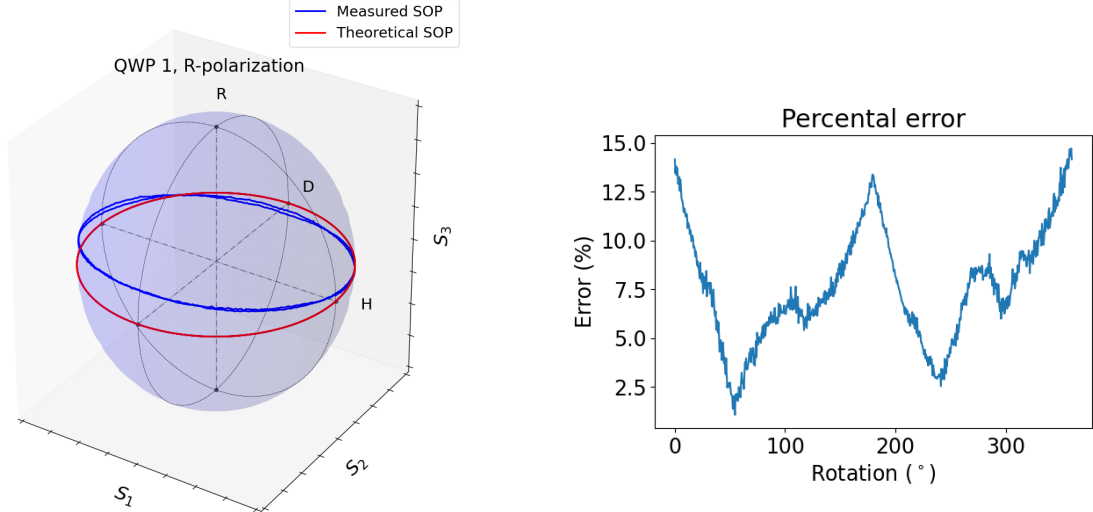


(a) The output SOP from the ideal QWP and the real QWP 1 visualised on the Poincaré sphere.

(b) The relative error in percent between the theoretical output SOP and the measured output SOP plotted versus the rotation angle of the QWP 1's rotation of the fast axis versus the horizontal axis.

Fig. 4.10: Characterisation of the QWP 1, where the input SOP has the L-state. The measured output SOP is compared with the output SOP produced by an ideal QWP.

Figure 4.10a shows that the output SOP produced by the QWP 1 from an L-polarised input SOP diverges from the theoretical output SOP. This divergence has the maximum at the surroundings of the vertical state on the Poincaré sphere. It can be observed in figure 4.10b that the maximal relative error is $22.961\% \pm 0.119\%$. The relative error is never reaching 0 % during this measurement. That is most likely since even if the plots of the measured SOP and the theoretical SOP intersect at the Poincaré sphere, so is these SOPs reached for different rotation angles.



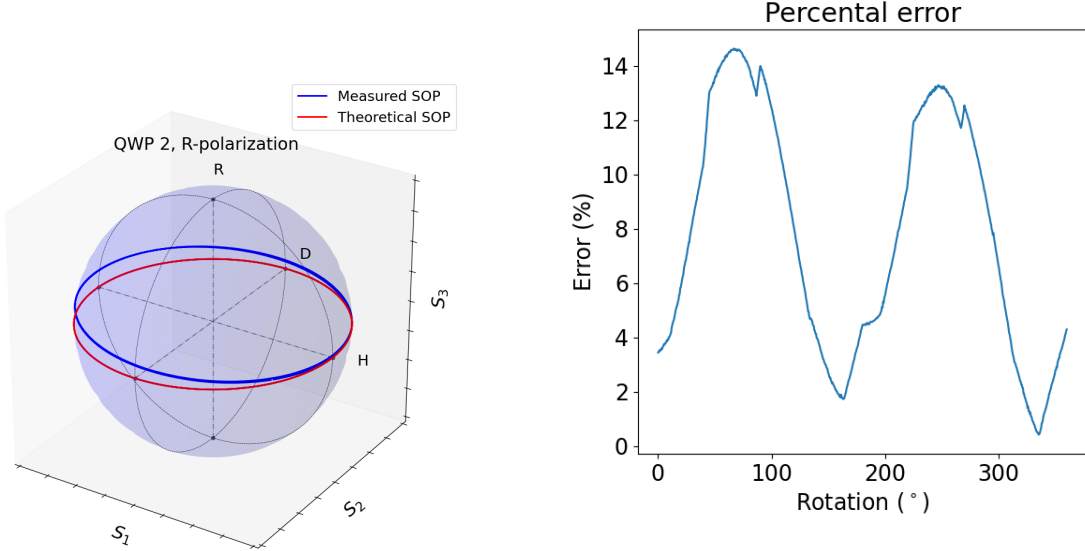
(a) The output SOP from the ideal QWP and the real QWP 1 visualised on the Poincaré sphere.

(b) The relative error in percent between the theoretical output SOP and the measured output SOP plotted versus the rotation angle of the QWP 1s rotation of the fast axis versus the horizontal axis.

Fig. 4.11: Characterisation of the QWP 1, where the input SOP has the R-state. The measured output SOP is compared with the output SOP produced by an ideal QWP.

Figure 4.11a shows that the output SOP produced by the QWP 1 when the input SOP is in the L-state diverges from the theoretical output SOP. Also for this state is the divergence maximal at the surroundings of the vertical state on the Poincaré sphere. The error plot is seen in figure 4.11b shows that the maximal difference is $14.727\% \pm 0.169\%$, which is noticeably smaller than the relative error for the L-state.

4.1.3 Characterisation of quarter waveplate 2

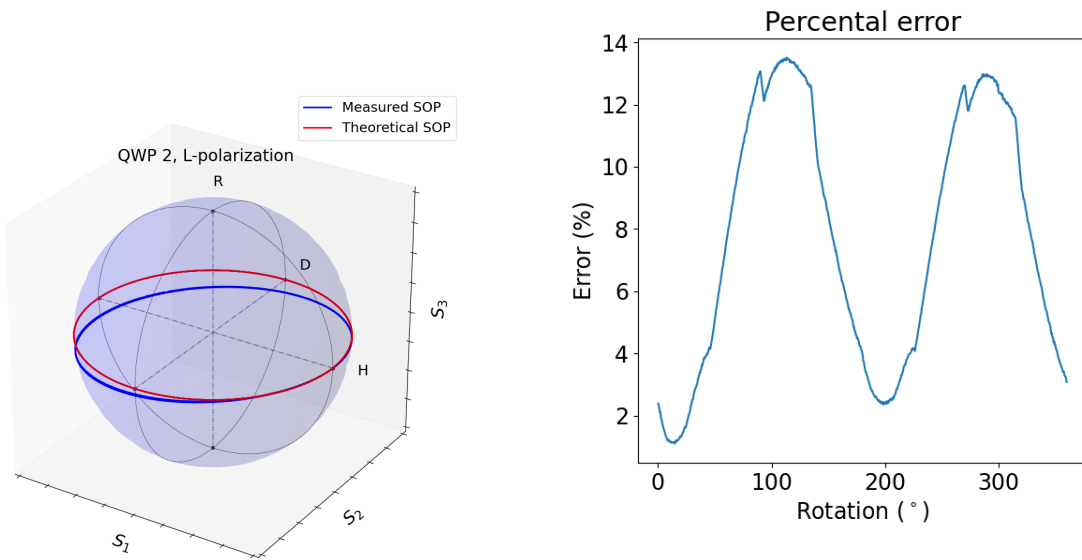


(a) The output SOP from the ideal QWP and the real QWP 2 visualised on the Poincaré sphere.

(b) The relative error in percent between the theoretical output SOP and the measured output SOP plotted versus the rotation angle of the QWP 2's rotation of the fast axis versus the horizontal axis.

Fig. 4.12: Characterisation of the QWP 2, where the input SOP has the R-state. The measured output SOP is compared with the output SOP produced by an ideal QWP.

Figure 4.12a shows that the output SOP produced by the QWP 2 from a R-polarised input SOP diverges from the theoretical output SOP. This divergence has its maximum at the surroundings of the vertical state on the Poincaré sphere. It is seen in figure 4.12b that the maximal difference is $14.622\% \pm 0.199\%$.

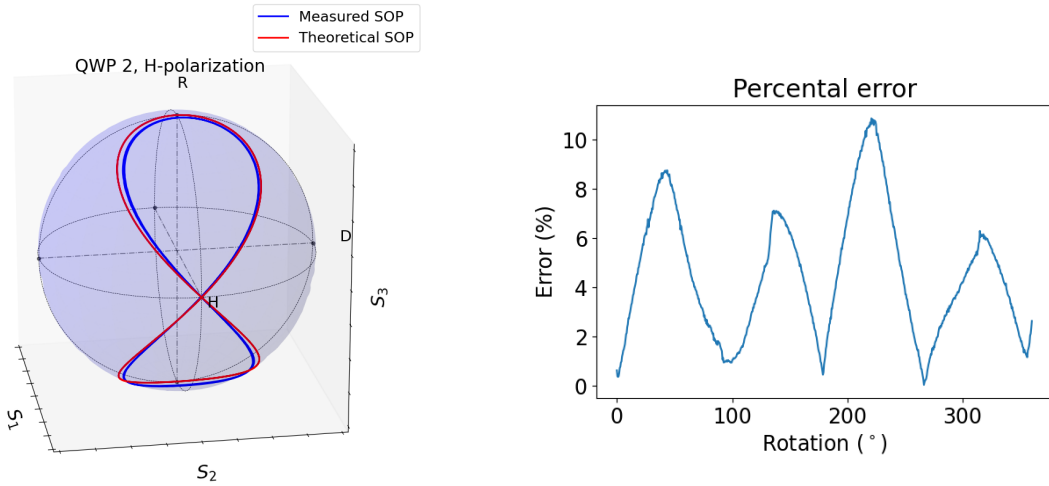


(a) The output SOP from the ideal QWP and the real QWP 2 visualised on the Poincaré sphere.

(b) The relative error in percent between the theoretical output SOP and the measured output SOP plotted versus the rotation angle of the QWP 2's rotation of the fast axis versus the horizontal axis.

Fig. 4.13: Characterisation of the QWP 2, where the input SOP is L-polarised. The measured output SOP is compared with the output SOP produced by an ideal QWP.

Figure 4.13a shows that the output SOP produced by the QWP 2 from a L-polarised input SOP diverges from the theoretical output SOP. The relative error has its maximum at the surroundings of the vertical state on the Poincaré sphere. As seen in figure 4.13b the maximum relative error is $13.509\% \pm 0.569\%$.

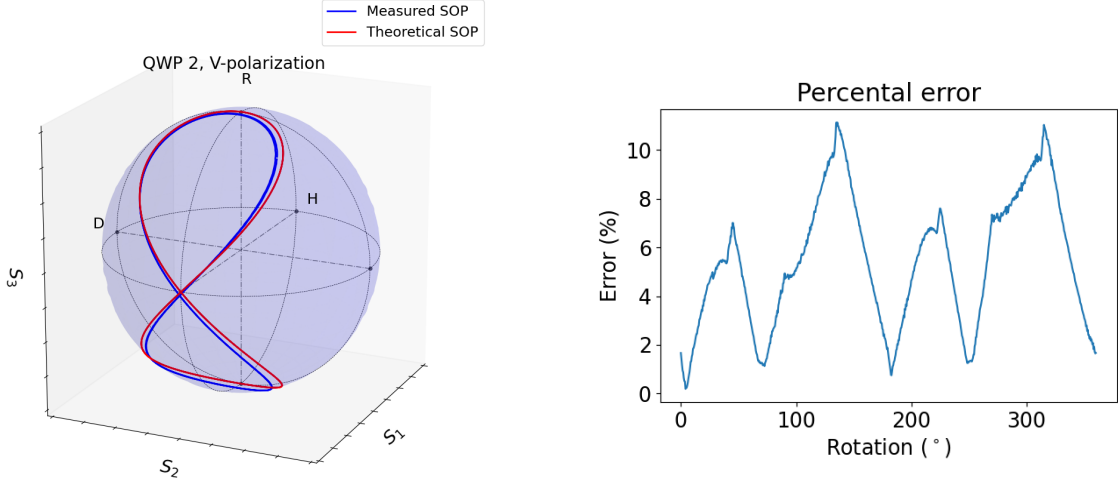


(a) The output SOP from the ideal QWP and the real QWP 2 visualised on the Poincaré sphere.

(b) The relative error in percent between the theoretical output SOP and the measured output SOP plotted versus the rotation angle of the QWP 2's rotation of the fast axis versus the horizontal axis.

Fig. 4.14: Characterisation of the QWP 2, where the input SOP has the H-state. The measured output SOP is compared with the output SOP produced by an ideal QWP.

Figure 4.14a shows how the output SOP produced by the QWP 2 from a H-polarised input SOP diverges from the theoretical output SOP. Although the divergence is noticeable, it seems to be reasonable. The error calculations plotted in figure 4.14b shows that the maximal difference is $10.874\% \pm 1.105\%$.



(a) The output SOP from the ideal QWP and the real QWP 2 visualised on the Poincaré sphere.

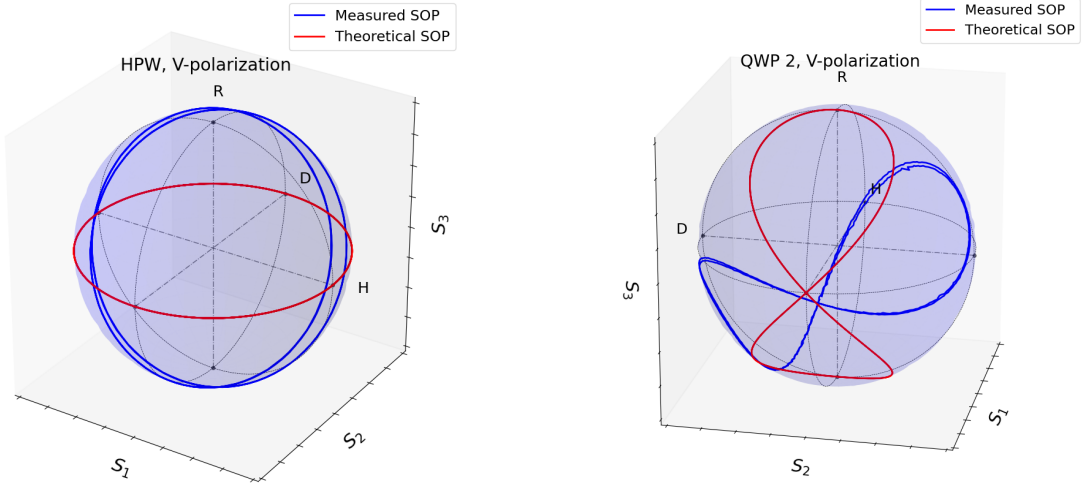
(b) The relative error in percent between the theoretical output SOP and the measured output SOP plotted versus the rotation angle of the QWP 2's rotation of the fast axis versus the horizontal axis.

Fig. 4.15: Characterisation of the QWP 2, where the input SOP has the V-state. The measured output SOP is compared with the output SOP produced by an ideal QWP.

Figure 4.15a shows that the output SOP produced by the QWP 2 from a V-polarised input SOP diverges from the theoretical output SOP. It is seen in figure 4.15b that the maximal relative error is $11.130\% \pm 0.194\%$.

From the characteristics of QWP1, HWP and QWP2 above, it is clear that the WPs are imperfect. The highest measured relative error between the theoretical output SOP from a perfect WP and the real WP is as high as $28.889\% \pm 0.519\%$, which the HWP generates. But also the QWP1 reaches a maximal relative error of $22.961\% \pm 0.119\%$, and QWP2 a maximum relative error of $14.622\% \pm 0.199\%$. If the light beam passes through all three WPs such that the relative errors are maximised, then the maximal total relative error between the theoretical output SOP for an ideal PC and the real PC is $81.657\% \pm 0.919\%$. This means that the algorithm used for the polarization control requires an error correcting function, which modifies the rotation of the WPs to compensate for the imperfections of the WPs. This error correcting function could either be analytical and based on the investigations of the imperfections of the WPs or by using a blind searching algorithm, which modifies the rotation angles such that the goal SOP is reached by trying to find the minimum error.

4.2 Waveplate characterisation using the final setup



(a) Characterisation of the HWP, the input SOP is in the V-state.

(b) Characterisation of the QWP 2, the input SOP is in the V-state.

Fig. 4.16: Characterisation of the HWP and QWP 2 using the final setup in Ericsson lab and a local laser.

In figure 4.16 are the results from using the final setup in Ericsson lab and a local laser seen. In figure 4.16a so are the input SOP turned to the V state, and in figure 4.16b to the V state. As seen in both figures, the measured SOP is rotated, compared to the theoretical output SOP. This phenomena is due to the setup sin in figure 4.16, with one notch and two mirrors reflecting the lightbeam. Each time the lightbeam is reflected are the SOP rotated. But due to the symmetry of the SOPs such that $\mathbf{SOP}(0^\circ) = \mathbf{SOP}(180^\circ)$ appears the SOP being rotated only a quarter, instead for three quarters. Of course if the non-symmetries induce by the imperfections in the WPs are ignored. This shows that the notch-filters works as expected, since the light is filtered according to the specifications, and the observations are consistent with the theory. However, compensating for this with an algorithm rotating the SOP to the correct values induces the complexity of the algorithm. The initial polarization control will therefor be performed with the setup seen in figure 3.4.

4.3 Polarization control

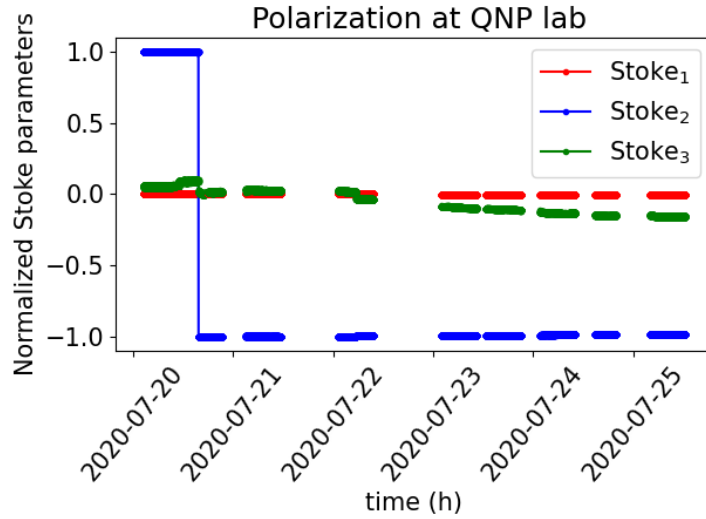
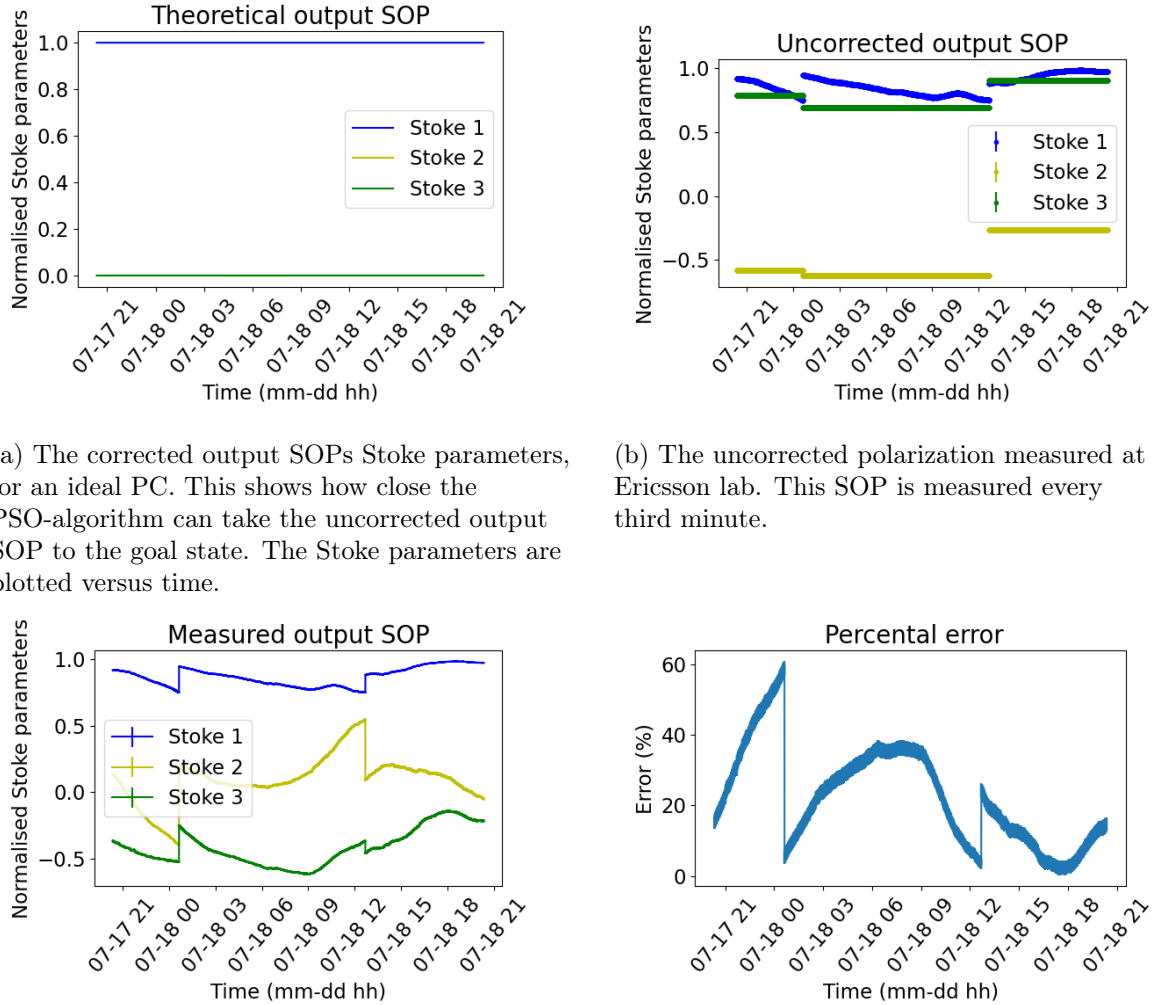


Fig. 4.17: The polarization of the input SOP, which is the original SOP. This is the normalised SOP of the lightbeam before it is sent through the fibre link to the Ericsson lab.

We notice how stable the initial SOP measured at QNP lab is in figure 4.17, except the turning from the H-state to the V-state the 20 July. This confirms that the polarization drift measured at Ericsson lab is induced by the birefringence in the fibre link, and not due to an unstable input SOP.



(a) The corrected output SOPs Stoke parameters, for an ideal PC. This shows how close the PSO-algorithm can take the uncorrected output SOP to the goal state. The Stoke parameters are plotted versus time.

(b) The uncorrected polarization measured at Ericsson lab. This SOP is measured every third minute.

(c) The corrected output SOP plotted with separate Stoke parameters versus the time. The polarization control is only changed when the relative error reaches a threshold value.

(d) The relative error in percent between the theoretical output SOP for ideal PC and the measured SOP, corrected with the real PC.

Fig. 4.18: The data for the correction of the polarization in a light beam, which has been sent from QNP lab to Ericsson lab, measured at Ericsson lab. The corrected output SOPs goal state is the H-state.

Figure 4.18a shows that it is theoretically possible to reach a perfect output SOP with the H-state from the uncorrected output SOP visualised in figure 4.18b. But when the WPs are rotated to a rotation angle calculated by the PSO-algorithm a perfect output SOP is not produced. This can be seen in figure 4.18c. Instead, the relative error between the theoretical output SOP and the measured output SOP is as high as $58.905\% \pm 1.938\%$ as shown in figure 4.18d.

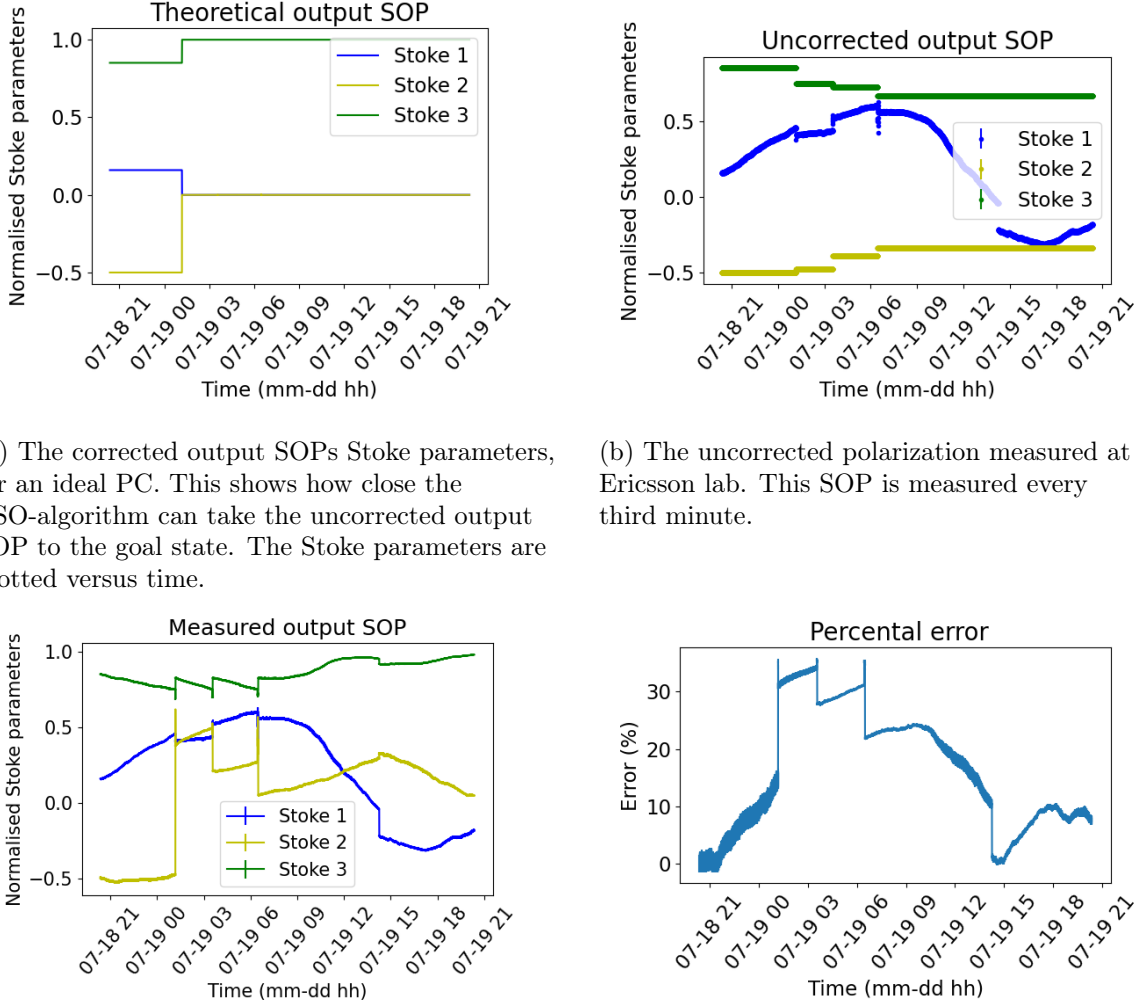
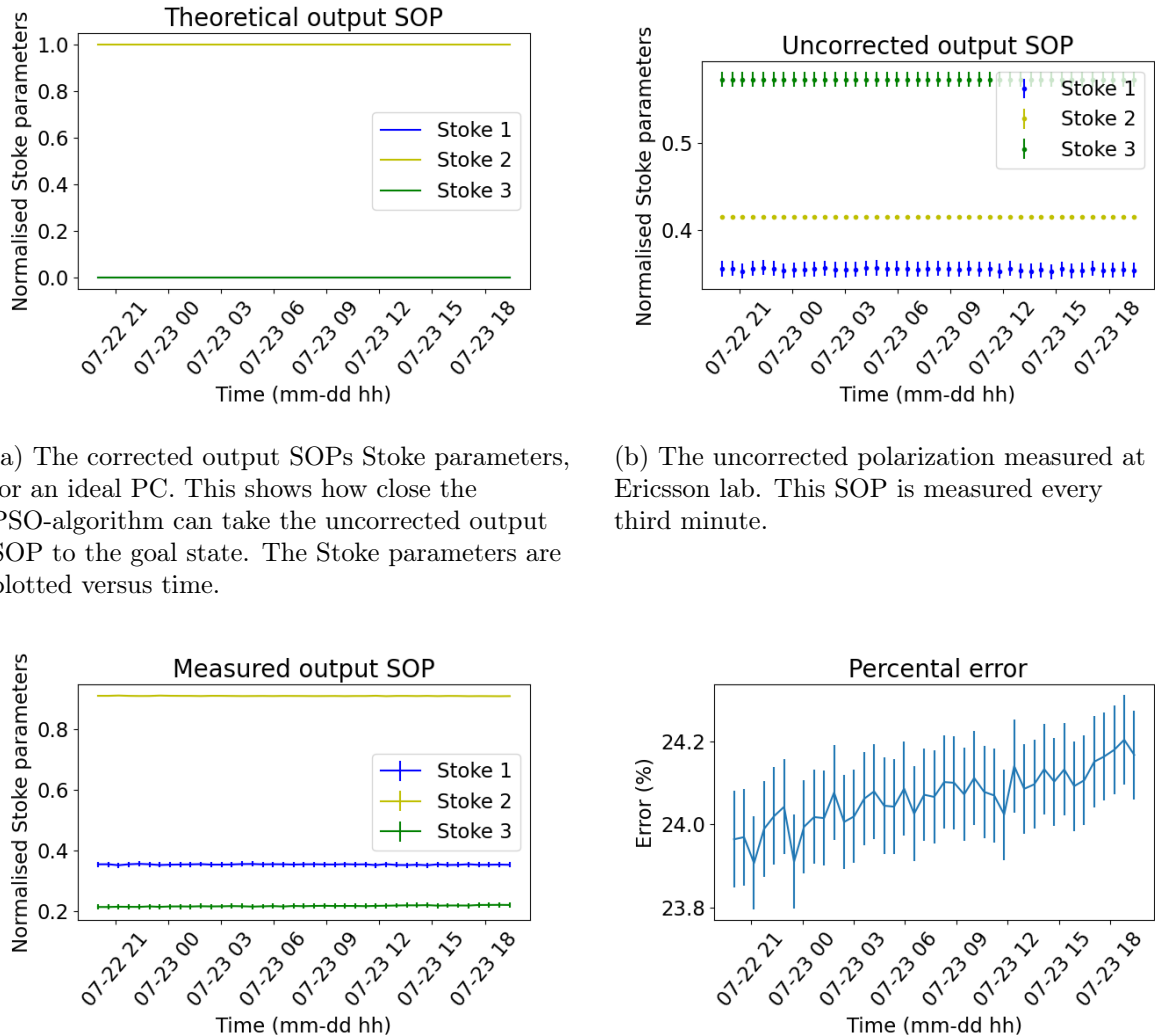


Fig. 4.19: The data for the correction of the polarization in a light beam, which has been sent from QNP lab to Ericsson lab, measured at Ericsson lab. The corrected output SOPs goal state is the R-state.

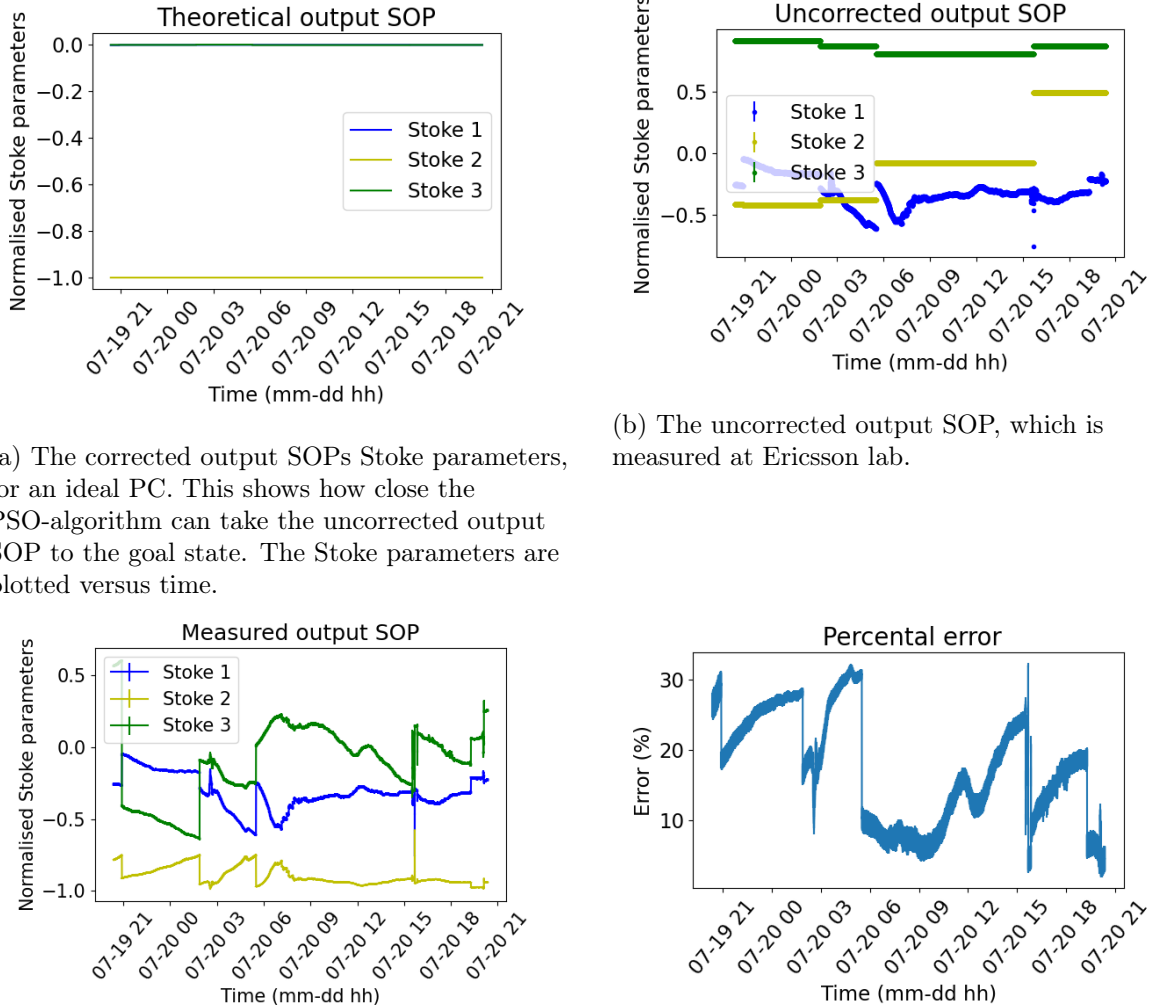
It can be seen in figure 4.19a that it is theoretically possible to reach a perfect output SOP with the A-state from the uncorrected output SOP visualised in figure 4.19b. However, the optimal values applied onto the real PC does not produce a perfect output SOP as seen in figure 4.19c. Instead is the relative error between the theoretical output SOP and the measured output SOP as high as $35.569\% \pm 0.245\%$ as seen in figure 4.19d.



(c) The corrected output SOP, plotted with separate Stoke parameters versus the time.
(d) The relative error in percent between the theoretical output SOP for ideal PC and the measured SOP, corrected with the real PC.

Fig. 4.20: The data for the correction of the polarization in a light beam, which has been sent from QNP lab to Ericsson lab, measured at Ericsson lab. The corrected output SOPs goal state is the D-state.

For the D-state, the output SOP is reasonable stable, as seen in figure 4.20c. However, the relative error between the theoretical output SOP seen in figure 4.20a and the real output SOP in figure 4.20c are still significant with a maximal error at $24.203\% \pm 0.107\%$ as seen in figure 4.20d. Although, the relative error is significant, the relative error is rather stable and changes only $\approx 0.2\%$ as seen in figure 4.20d.



(a) The corrected output SOPs Stoke parameters, for an ideal PC. This shows how close the PSO-algorithm can take the uncorrected output SOP to the goal state. The Stoke parameters are plotted versus time.

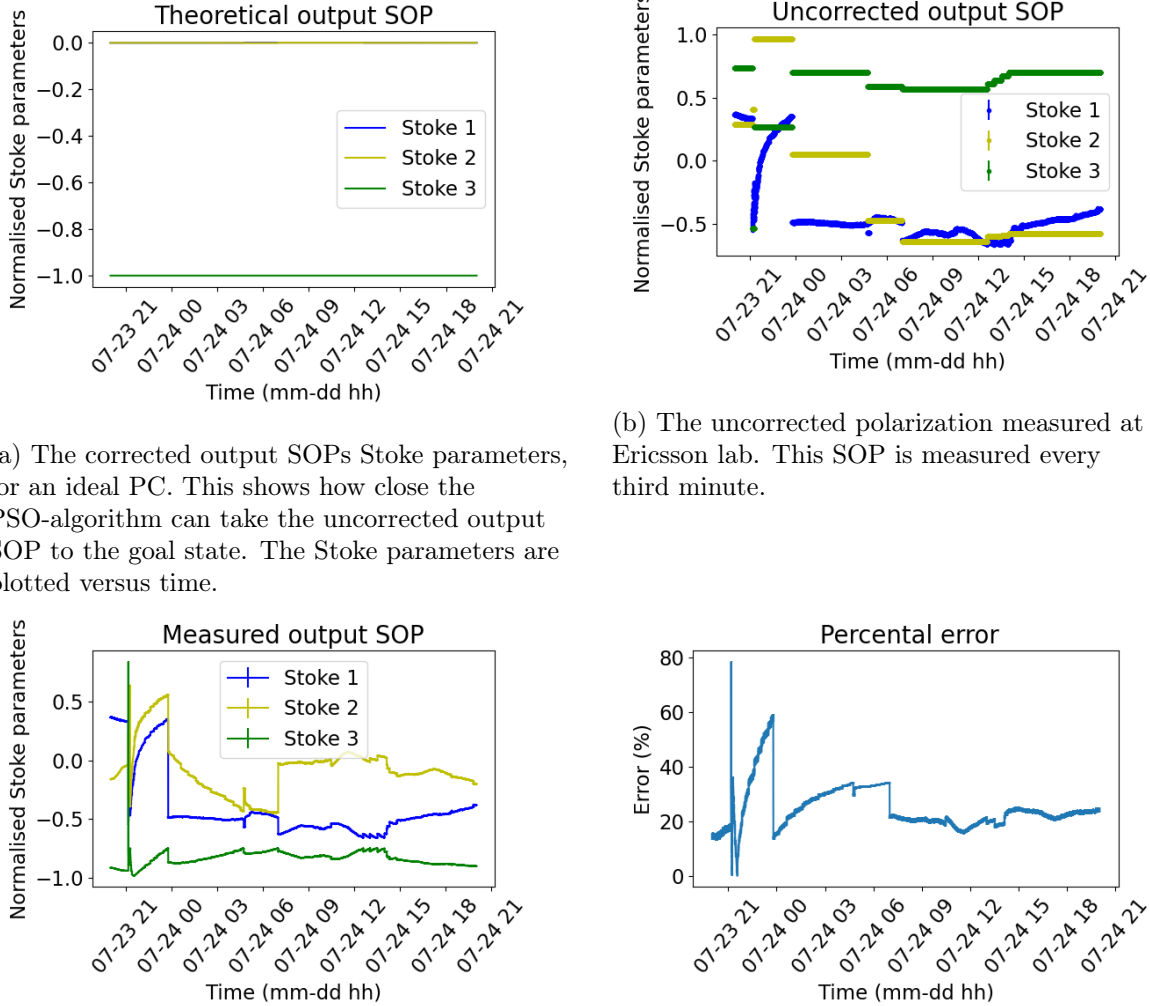
(b) The uncorrected output SOP, which is measured at Ericsson lab.

(c) The corrected output SOP, plotted with separate Stoke parameters versus the time.

(d) The relative error in percent between the theoretical output SOP for ideal PC and the measured SOP, corrected with the real PC. The relative error is plotted against the time.

Fig. 4.21: The data for the correction of the polarization in a light beam, which has been sent from QNP lab to Ericsson lab, measured at Ericsson lab. The corrected output SOPs goal state is the A-state.

It can be seen in figure 4.21a that it is theoretically possible to reach a perfect output SOP with the A-state from the uncorrected output SOP visualised in figure 4.21b. However, the optimal values applied onto the real PC does not produce a perfect output SOP as seen in figure 4.21c. Instead is the relative error between the theoretical output SOP and the measured output SOP as high as $31.978\% \pm 1.796\%$, as seen in figure 4.21d.



(a) The corrected output SOPs Stoke parameters, for an ideal PC. This shows how close the PSO-algorithm can take the uncorrected output SOP to the goal state. The Stoke parameters are plotted versus time.

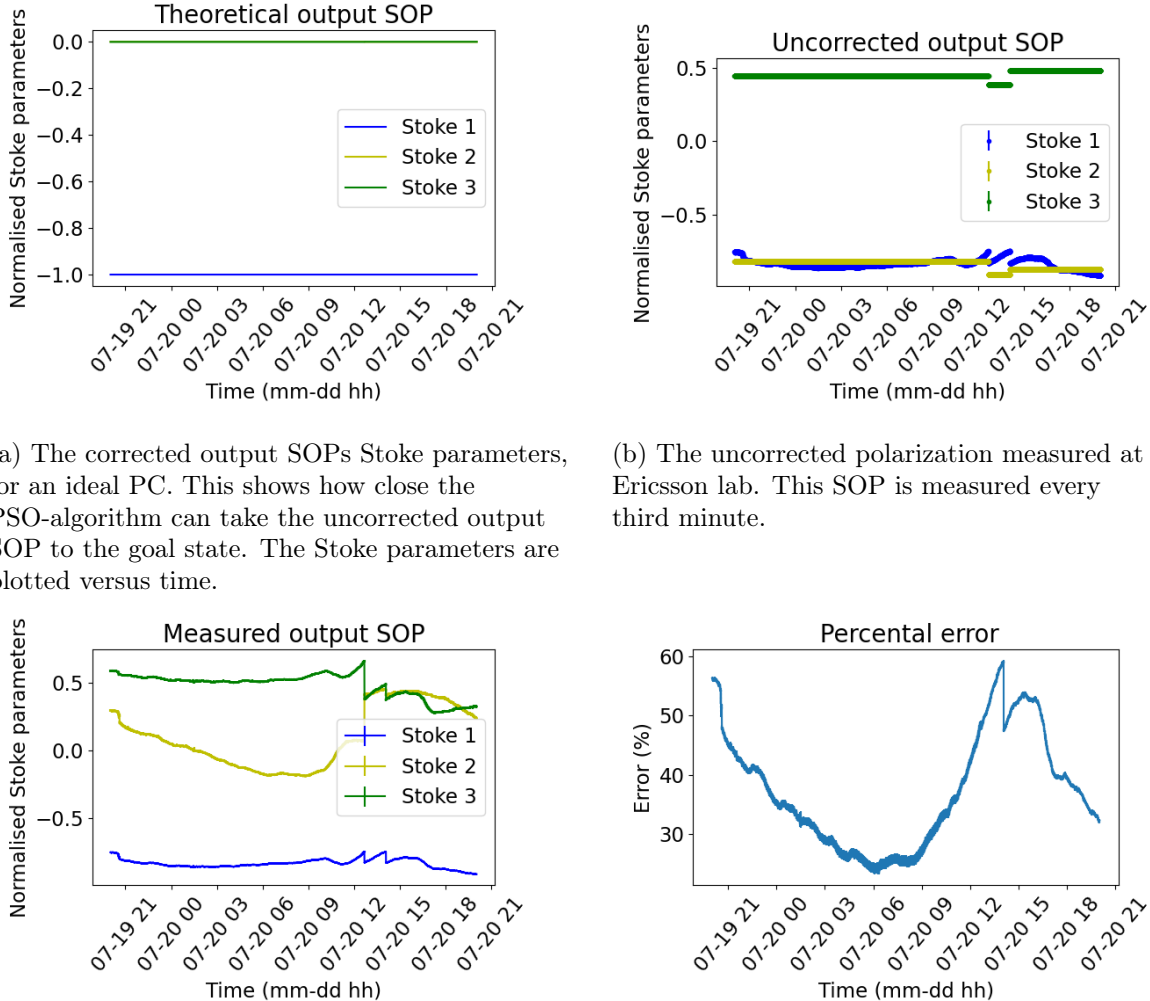
(b) The uncorrected polarization measured at Ericsson lab. This SOP is measured every third minute.

(c) The corrected output SOP, plotted with separate Stoke parameters versus the time. The polarization control is only changed when the relative error reaches a threshold value. Hence the SOP drifts freely as long as the threshold value is not reached, and might change drastically when the polarization control is activated.

(d) The relative error in percent between the theoretical output SOP for ideal PC and the measured SOP, corrected with the real PC. The maximal error is $78.08739\% \pm 0.222\%$, which is very close to the maximal possible relative error of $\approx 81\%$, calculated from the individual waveplates maximal relative error.

Fig. 4.22: The data for the correction of the polarization in a light beam, which has been sent from QNP lab to Ericsson lab, measured at Ericsson lab, measured at Ericsson lab. The corrected output SOPs goal state is the L-state.

As previous observations, it can be seen in figure 4.22a that it is theoretically possible to reach a perfect output SOP with the L-state from the uncorrected output SOP visualised in figure 4.22b. However, the optimal values applied onto the real PC does not produce a perfect output SOP as seen in figure 4.22c. The relative error is instead high as $78.087\% \pm 0.222\%$ as seen in figure 4.22d. This is close to the maximal possible relative error of $\sim 81\%$.



(c) The corrected output SOP, plotted with separate Stoke parameters versus the time. The polarization control is only changed when the relative error reaches a threshold value.

(d) The relative error in percent between the theoretical output SOP for ideal PC and the measured SOP, corrected with the real PC. The maximal error is $59.281\% \pm 1.15\%$.

Fig. 4.23: The data for the correction of the polarization in a lightbeam, which have been sent from QNP lab to Ericsson lab, measured at Ericsson lab, measured at Ericsson lab. The corrected output SOPs goal state is the V-state.

Also for the goal SOP to be the V-state is the difference between the theoretical output seen in figure 4.23a and the measured corrected output SOP seen in figure 4.23c noticeable. The relative error reaches its maximum at $59.281\% \pm 1.15\%$ as seen in figure 4.23d, which is a lot higher than its supposed to be.

The data displayed in figures 4.18 - 4.23 shows that it is theoretically possible to turn the SOP such that all the pure states can be achieved with the PSO-algorithm, but modifications are required for satisfying results with the real imperfect WPs. To produce a better output SOP the function for minimisation must be modified such that it reflects the real WPs. Another observation is the drift of the corrected output SOP, which drifts freely within the threshold value of the relative error. Therefore the corrected output SOP is not stable, which requires a stabilisation algorithm. Since the function for minimisation is flexible, the stabilisation algorithm could also be based on the PSO-algorithm. Specifically, since the current algorithm shows good results for the ideal WPs implies that a modification of the current function for minimisation together with a lower threshold value are the only required changes.

One can notice by studying previous results for polarization control that it seems like it has been multiple successful implementations of QKD when using polarization controlling setups. One of these was when Treiber *et al.* 2009 reported successful polarization control and implementation of the BBM92-protocol, which is a protocol similar to the BB84-protocol, using electro-optical polarization controllers in a laboratory environment [27]. However, another implementation of polarization control for QKD has been reported successful. One of these was reported in 2018 when Li *et al.* successfully implemented polarization stabilisation in aerial fibre. With this method based on the Downhill Simplex Algorithm and using electro-optical polarization controllers [28]. These two successful reports of QKD used electro-optical polarization controllers. That did also Xiang *et al.*, which report measurements proving entanglement from on-demand generated photons in deployed fibre in Cambridge city [11]. However, electro-optical polarization controllers reduces the light too much for the implementation of QKD using quantum dot generated photons. Therefore are free space polarization controllers a better option for polarization control intended for QKD. One successful implementation of free space polarization control was reported the current year. For this implementation was a simplex-algorithm method used when Schimpf *et al.* implemented the BBM92-protocol During this implementation was the photon density matrix constructed and used for the minimisation function [29]. Although, this was proved an efficient method in a laboratory environment, this method is not feasible for deployed fibre in a changing environment. Since the photon density matrix must be remeasured every time the SOP changes, which it does continuously outside lab environment. Therefore can the SOP potentially change too much during the construction of the density matrix. This construction would also result in much data being lost to the matrix construction.

Chapter 5

Conclusion and outlook

The aim of this work is the correction of the polarization drift induced by the optical fibre link between QNP lab at KTH and Ericsson lab in Kista. It has been shown that the polarization drifts induced by the optical link between the QNP lab and Ericsson lab are slow. Hence is not time a critical component in the design of the polarization controlling system. Further measurements showed that the combined errors of the WPs used for the polarization controlling setup give a maximum possible error of $\sim 81\%$. Therefore, the algorithm used for polarization control should be simple to adjust for imperfect WPs. However, the results shows that a stabilisation algorithm, as well as some form of error compensation, is required before the polarization control is satisfying.

The error compensation could be performed with help of changing the transmission matrix from the transmission matrix for ideal WPs, to a matrix which describes the polarization controllers WPs. A method for characterisation of WPs such that a Mueller Matrix can be constructed from these and has been described by Honggang *et al.* [30]. If the polarization controllers retardation properties could be accurately described with the transmission matrix, which could be used in the function of minimisation the polarization control would improve. This matrix could also be used to construct a polarization stabilising algorithm where the nature of the changing medium and the uncorrected output SOP is known, via stabilisation methods such as the gradient method. But it is also possible to base a polarization stabilising algorithm on the PSO-algorithm and a function for minimisation which rather stabilised the SOP than rotate it. This would as an example be possible by using dynamic eigenstates (DES), which can be derived from the Jones matrices. These eigenstates can be used to predict how a WP influences the output SOP [31]. The DES-vectors only exist in a single pair for each control parameter and are manifested as the central axis of the SOP evolution. Hence, the DES-vector can be found via the cross product of two vectors in the plane of evolution [32].

Implementations of QKD in fibre are under continuous development, and new achievements are continuously reached. As already mentioned, in 2019 entanglement between on-demand generated photons could be proved in a 96 km underwater deployed fibre [33]. A satisfying polarization control at Ericsson lab would enable single photon measurements and entanglement measurements of photons generated with quantum dots as a first step. It would in the near future, enable a possibility of implementing the BB84-protocol and E91-protocol using a discrete spectrum in deployed fibre.

The fibre link is also under the process of expansion to a fibre network with a link connecting Telenor in Solna to Ericsson lab in Kista and QNP lab at KTH. This would create a fibre network

with three nodes, the QNP lab at KTH, Ericsson lab in Kista and Telenor lab in Solna. This could be used as a prototype quantum network and enable implementations of three-part quantum communication protocols. This kind of network can in the future also be used as the first long-distance network connecting quantum computers. This is actualised since Google declared quantum supremacy, which indicates that the importance of as well as transferring information in quantum states as QKD will increase [34].

Bibliography

- [1] Driva eget solna bäst i sverige för företag. <https://driva-eget.se/nyheter/solna-bast-i-sverige-for-foretag/>. Accessed: 2020-07-10.
- [2] G. S Vernam. Cipher printing telegraph systems for secret wire and radio telegraphic communications. *Transactions of the American Institute of Electrical Engineers*, XLV:295–301, 1926.
- [3] Claude E Shannon. *The mathematical theory of communication*. Univ. of Illinois P., Urbana, Ill., 1949.
- [4] W. K Wootters and W. H Zurek. A single quantum cannot be cloned. *Nature (London)*, 299(5886):802–803, 1982.
- [5] Charles H. Bennett and Gilles Brassard. Quantum cryptography: Public key distribution and coin tossing. *Theoretical Computer Science*, 560(1):7–11, 2014.
- [6] Artur K Ekert. Quantum cryptography based on bell’s theorem. *Physical review letters*, 67(6):661–663, 1991.
- [7] Valerio Scarani, Helle Bechmann-Pasquinucci, Nicolas J. Cerf, Miloslav Dusek, Norbert Lütkenhaus, and Momtchil Peev. The security of practical quantum key distribution.(report). *Reviews of Modern Physics*, 81(3):1301–1350, 2009.
- [8] H. J Kimble. The quantum internet. *Nature (London)*, 453(7198):1023–1030, 2008.
- [9] J F Dynes, H Takesue, Z L Yuan, A W Sharpe, K Harada, T Honjo, H Kamada, O Tadanaga, Y Nishida, M Asobe, and A J Shields. Efficient entanglement distribution over 200 kilometers. *Optics express*, 17(14):11440–11449, 2009.
- [10] Xiang Zhao, Joy Louveau, Jacob Chamoun, and Michel J. F Digonnet. Thermal sensitivity of the birefringence of air-core fibers and implications for the rfog. *Journal of Lightwave Technology*, 32(14):2577–2581, 2014.
- [11] Z. H. Xiang, J. Huwer, R. M. Stevenson, J. Skiba Szymanska, M. B. Ward, I. Farrer, D. A. Ritchie, and A. J. Shields. Long-term transmission of entangled photons from a single quantum dot over deployed fiber. 2019.
- [12] Sören Wengerowky, Siddarth Koduru Joshi, Fabian Steinlechner, Julien Zichi, Sergiy M. Dobrovolskiy, René van der Molen, Johannes W. N. Los, Val Zwillaer, Marijn A. M. Versteegh, Alberto Mura, Davide Calonico, Massimo Inguscio, Hannes Hübel, Liu Bo, Thomas Scheidl, Anton Zeilinger, André Xuereb, and Rupert Ursin. Entanglement distribution over 96-km-long submarine optical fiber. *Proceedings Of The National Academy Of Sciences Of The United States Of America*, 116(14), 2019.

- [13] Edward Collett. *Field Guide to Polarization*. FG05. 1st ed.. edition, 2004.
- [14] Robert Fickler. *Quantum Entanglement of Complex Structures of Photons*. Springer Theses, Recognizing Outstanding Ph.D. Research. 1st ed. 2016.. edition, 2016.
- [15] N.G Walker and G.R Walker. Polarization control for coherent communications. *Journal of Lightwave Technology*, 8(3):438–458, 1990.
- [16] Introduction to waveplates. <https://www.newport.com/n/introduction-to-waveplates>. Accessed: 2020-02-20.
- [17] R Simon and N Mukunda. Minimal three-component su(2) gadget for polarization optics. *Physics Letters A*, 143(4):165–169, 1990.
- [18] F Heismann. Analysis of a reset-free polarization controller for fast automatic polarization stabilization in fiber-optic transmission systems. *Journal of Lightwave Technology*, 12(4):690–699, 1994.
- [19] M Martinelli and R.A Chipman. Endless polarization control algorithm using adjustable linear retarders with fixed axes. *Journal of Lightwave Technology*, 21(9):2089–2096, 2003.
- [20] Torkel Glad. *Reglerteknik : grundläggande teori*. Studentlitteratur, Lund, 4., [omarb.] uppl.. edition, 2006.
- [21] Joaquim D. Garcia and Gustavo C. Amaral. An optimal polarization tracking algorithm for lithium-niobate-based polarization controllers. 2016.
- [22] Xue Yuan, Yang Zhang, Ming Zhang, Jin Zhang, and Yong Huang. Adaptive polarization stabilization with dspo algorithm in optical communication system. *Applied Mechanics and Materials*, 48-49:139, 2011.
- [23] J Kennedy and R Eberhart. Particle swarm optimization. In *Proceedings of ICNN'95 - International Conference on Neural Networks*, volume 4, pages 1942–1948 vol.4. IEEE, 1995.
- [24] Thorlabs. Pax1000 operation manual.
- [25] Thorlabs. Pax5710 operation manual.
- [26] Joshua A. Jones, Anthony J. D'Addario, Brett L. Rojec, G. Milione, and Enrique J. Galvez. The poincare-sphere approach to polarization: formalism and new labs with poincare beams.(author abstract). *American Journal of Physics*, 84(11):822, 2016.
- [27] Alexander Treiber, Andreas Poppe, Michael Hentschel, Daniele Ferrini, Thomas Lorünser, Edwin Querasser, Thomas Matyus, Hannes Hübel, and Anton Zeilinger. Afully automated entanglement-based quantum cryptography system for telecom fiber networks. *New Journal of Physics*, 11(4):045013, 2009.
- [28] Dong-Dong Li, Song Gao, Guo-Chun Li, Lu Xue, Li-Wei Wang, Chang-Bin Lu, Yao Xiang, Zi-Yan Zhao, Long-Chuan Yan, Zhi-Yu Chen, Gang Yu, and Jian-Hong Liu. Field implementation of long-distance quantum key distribution over aerial fiber with fast polarization feedback. *Optics express*, 26(18):22793–22800, 2018.

- [29] Christian Schimpf, Marcus Reindl, Daniel Huber, Barbara Lehner, Saimon F. Covre Da Silva, Santanu Manna, Michal Vyvlecka, Philip Walther, and Armando Rastelli. Quantum cryptography with highly entangled photons from semiconductor quantum dots. 2020.
- [30] Honggang Gu, Xiuguo Chen, Yating Shi, Hao Jiang, Chuanwei Zhang, Peng Gong, and Shiyuan Liu. Comprehensive characterization of a general composite waveplate by spectroscopic mueller matrix polarimetry. *Optics express*, 26(19):25408, 2018.
- [31] W Shieh and H Kogelnik. Dynamic eigenstates of polarization. *IEEE Photonics Technology Letters*, 13(1):40–42, 2001.
- [32] William La. Polarization model and control in fiber-based bidirectional systems with reflections. Master’s thesis, University of Toronto, 2010.
- [33] Sören Wengerowsky, Siddarth Koduru Joshi, Fabian Steinlechner, Julien R Zichi, Sergiy M Dobrovolskiy, René van der Molen, Johannes W N Los, Val Zwiller, Marijn A M Versteegh, Alberto Mura, Davide Calonico, Massimo Inguscio, Hannes Hübel, Liu Bo, Thomas Scheidl, Anton Zeilinger, André Xuereb, and Rupert Ursin. Entanglement distribution over a 96-km-long submarine optical fiber. *Proceedings of the National Academy of Sciences - PNAS*, 116(14):6684–6688, 2019.
- [34] Frank Arute, Kunal Arya, Ryan Babbush, Dave Bacon, Joseph C Bardin, Rami Barends, Rupak Biswas, Sergio Boixo, Fernando G. S. L Brando, David A Buell, Brian Burkett, Yu Chen, Zijun Chen, Ben Chiaro, Roberto Collins, William Courtney, Andrew Dunsworth, Edward Farhi, Brooks Foxen, Austin Fowler, Craig Gidney, Marissa Giustina, Rob Graff, Keith Guerin, Steve Habegger, Matthew P Harrigan, Michael J Hartmann, Alan Ho, Markus Hoffmann, Trent Huang, Travis S Humble, Sergei V Isakov, Evan Jeffrey, Zhang Jiang, Dvir Kafri, Kostyantyn Kechedzhi, Julian Kelly, Paul V Klimov, Sergey Knysh, Alexander Korotkov, Fedor Kostritsa, David Landhuis, Mike Lindmark, Erik Lucero, Dmitry Lyakh, Salvatore Mandrà, Jarrod R McClean, Matthew McEwen, Anthony Megrant, Xiao Mi, Kristel Michelsen, Masoud Mohseni, Josh Mutus, Ofer Naaman, Matthew Neeley, Charles Neill, Murphy Yuezhen Niu, Eric Ostby, Andre Petukhov, John C Platt, Chris Quintana, Eleanor G Rieffel, Pedram Roushan, Nicholas C Rubin, Daniel Sank, Kevin J Satzinger, Vadim Smelyanskiy, Kevin J Sung, Matthew D Trevithick, Amit Vainsencher, Benjamin Villalonga, Theodore White, Z. Jamie Yao, Ping Yeh, Adam Zalcman, Hartmut Neven, and John M Martinis. Quantum supremacy using a programmable superconducting processor. *Nature (London)*, 574(7779):505–510, 2019.

